The Astrophysical Journal, 659:29–51, 2007 April 10


# *CHANDRA* MULTIWAVELENGTH PROJECT X-RAY POINT SOURCE NUMBER COUNTS AND THE COSMIC X-RAY BACKGROUND

Minsun Kim,[1,2] Belinda J. Wilkes,[1] Dong-Woo Kim,[1] Paul J. Green,[1] Wayne A. Barkhouse,[3] Myung Gyoon Lee,[2] John D. Silverman,[4] and Harvey D. Tananbaum[1]

*Received 2006 April 24; accepted 2006 November 20*

## ABSTRACT

We present the *Chandra* Multiwavelength Project (ChaMP) X-ray point source number counts and cosmic X-ray background (CXRB) flux densities in multiple energy bands. From the ChaMP X-ray point source catalog, ∼5500 sources are selected, covering 9.6 deg$^2$ in sky area. To quantitatively characterize the sensitivity and completeness of the ChaMP sample, we perform extensive simulations. We also include the ChaMP+CDFs (Chandra Deep Fields) number counts to cover large flux ranges from $2 \times 10^{-17}$ to $2.4 \times 10^{-12}$ (0.5–2 keV) and from $2 \times 10^{-16}$ to $7.1 \times 10^{-12}$ (2–8 keV) ergs cm$^{-2}$ s$^{-1}$. The ChaMP and the ChaMP+CDFs differential number counts are well fitted with a broken power law. The best-fit faint and bright power indices are $1.49 \pm 0.02$ and $2.36 \pm 0.05$ (0.5–2 keV), and $1.58 \pm 0.01$ and $2.59^{+0.06}_{-0.05}$ (2–8 keV), respectively. We detect breaks in the differential number counts that appear at different fluxes in different energy bands. Assuming a single power-law model for a source spectrum, we find that the same population(s) of soft X-ray sources causes the break in the differential number counts for all energy bands. We measure the resolved CXRB flux densities from the ChaMP and the ChaMP+CDFs number counts with and without bright target sources. By adding the known unresolved CXRB to the ChaMP+CDF resolved CXRB, we also estimate total CXRB flux densities. The fractions of the resolved CXRB without target sources are $78\% \pm 1\%$ and $81\% \pm 2\%$ in the 0.5–2 and 2–8 keV bands, respectively, somewhat lower than but generally consistent with earlier numbers because of their large errors. These fractions increase by ∼1% when target sources are included.

*Subject headings:* cosmology: observations — methods: data analysis — surveys — X-rays: diffuse background — X-rays: general

*Online material:* color figures

## 1. INTRODUCTION

What is the origin and nature of the cosmic X-ray background (CXRB)? Can detected X-ray sources account for the CXRB? The CXRB consists of resolved and unresolved components. The resolved CXRB originates in discrete sources such as point and extended sources, while diffuse components and faint sources that are below current flux limits contribute to the unresolved CXRB. The contribution of discrete X-ray sources to the CXRB can be directly measured from their number counts. Using the deep surveys of *ROSAT* (*Röntgensatellit*), *Chandra*, and *XMM-Newton*, the X-ray number counts have been determined down to flux limits of $\sim 2.3 \times 10^{-17}$ (0.5–2 keV), $\sim 2.0 \times 10^{-16}$ (2–8 keV), and $\sim 1.2 \times 10^{-15}$ (5–10 keV) ergs cm$^{-2}$ s$^{-1}$, and ≈80%–90% of the CXRB is resolved into discrete X-ray sources in the 0.5–2 and 2–8 keV bands (see Brandt & Hasinger 2005 for a detailed review). In this study, using the *Chandra* Multiwavelength Project (ChaMP) and the Chandra Deep Fields (CDFs) data, which include the largest number of sources and cover the widest sky area and flux range from a single satellite (*Chandra*) to date, we provide statistically robust X-ray number counts and CXRB flux densities without the cross calibration problem that is usually included in data from multiple satellites. We also study the X-ray number counts in multiple energy bands to systematically understand their behavior in each energy band.

There have been many similar studies. Using the *Chandra* survey of SSA13, Mushotzky et al. (2000) presented the X-ray number counts in the 0.5–2 and 2–10 keV bands and suggested that detected hard X-ray sources account for at least 75% of the hard CXRB and that the mean X-ray spectrum of these sources is in good agreement with that of the background. Cowie et al. (2002) presented the 2–8 keV number counts from the Chandra Deep Field–South (CDF-S) and Chandra Deep Field–North (CDF-N) with SSA13/SSA22, and Rosati et al. (2002) presented those of the CDF-S, finding that at most ∼10% (∼15%) of the CXRB is unresolved in the soft (hard) energy band. Manners et al. (2003) presented the X-ray number counts in the 0.5–2, 2–8, and 0.5–8 keV bands using the ELAIS (European Large-Area *ISO* [*Infrared Space Observatory*] Survey) data. Moretti et al. (2003, hereafter M03) presented the X-ray number counts in the 0.5–2 and 2–10 keV bands from combining data from three different surveys (*ROSAT*, *Chandra*, and *XMM-Newton*). They concluded that 95% and 89% of the soft and hard CXRB, respectively, can be resolved into discrete X-ray sources. Bauer et al. (2004, hereafter B04) combined the CDF-N and CDF-S data and measured the contributions of the faint X-ray source populations to the CXRB. They found that 90% (0.5–2 keV) and 93% (2–8 keV) of the total CXRB was resolved into discrete sources. Basilakos et al. (2005) presented the number counts of the *XMM-Newton*/Two Degree Field (2dF) survey in the 0.5–2 and 0.5–8 keV bands, and Chiappetti et al. (2005) presented the number counts of the *XMM-Newton* Large-Scale Structure (LSS) survey in the 0.5–2 and 2–10 keV bands. Worsley et al. (2005) found that the resolved fractions of the CXRB are ∼85% (0.5–2 keV), ∼80% (2–10 keV), and ∼50% at ≳8 keV. Recently, Hickox & Markevitch (2006, hereafter HM06) directly measured the absolute unresolved CXRB

[1] Harvard-Smithsonian Center for Astrophysics, Cambridge, MA.
[2] Department of Physics and Astronomy, Astronomy Program, Seoul National University, Seoul, Korea.
[3] Department of Astronomy, University of Illinois at Urbana-Champaign, Urbana, IL.
[4] Max-Planck-Institut für extraterrestrische Physik, Garching, Germany.

TABLE 1
Definition of Energy Bands

| Band | Definition (keV) |
|---|---|
| **Broad** | |
| B | 0.3–8 |
| Bc | 0.5–8 |
| **Soft** | |
| S | 0.3–2.5 |
| Sc | 0.5–2 |
| Ss[a] | 1–2 |
| **Hard** | |
| H | 2.5–8 |
| Hc | 2–8 |
| He[b] | 2–10 |

[a] The Ss (2–10 keV) band was used only for estimating the CXRB flux density (see § 6).
[b] The He (2–10 keV) band was not used in this study; however, it is referred to in previous studies.

from Chandra Deep Field images after excluding point and extended sources in those fields. They also estimated the resolved X-ray source intensity from the CDFs and from the number counts for brighter sources (Vikhlinin et al. 1995; M03), and then estimated the total CXRB flux density by combining the two. They found that the resolved fractions of the CXRB are 77% ± 3% (1–2 keV) and 80% ± 8% (2–8 keV). Until now, using the *ROSAT*, *XMM-Newton*, and *Chandra* data, these studies have revealed that ∼80% of the CXRB is resolved into discrete X-ray sources in the 0.5–2 and 2–8 keV bands; however, the resolved fraction of the CXRB significantly decreases at ≳8 keV.

The ChaMP is a serendipitous, wide-area survey covering intermediate and high fluxes using *Chandra* archival data. Kim et al. (2004a) presented the initial ChaMP catalog, which contains ∼800 X-ray point sources in the central region of 62 of 149 ChaMP fields. From the initial ChaMP catalog, Kim et al. (2004b, hereafter KD04) presented X-ray number counts in the 0.5–2 and 2–8 keV bands. To avoid the incompleteness of the selected fields, they selected sources having large X-ray source counts (>20) and located close to on-axis (<400″). The selected sample covered ∼1.1 deg$^2$ in sky area. In the flux range from $10^{-15}$ to $10^{-13}$ ergs cm$^{-2}$ s$^{-1}$ (0.5–2 keV), they detected the break in the differential number counts. However, due to the shallow flux limit, they could not detect the break in the 2–8 keV band.

In this study, we use the latest ChaMP X-ray point source catalog, which contains ∼6800 X-ray point sources in 149 ChaMP fields with sky coverage area of ∼10 deg$^2$ (Kim et al. 2007, hereafter KM07) to determine the X-ray point source number counts in six energy bands. To correct for incompleteness, Eddington bias, and instrumental effects, and to include large off-axis angles (up to ∼15′) and faint (down to ∼5 source counts) sources, we perform extensive simulations to calculate the sky coverage of the selected sources as a function of flux. Using this large sample and the simulation results, we present the X-ray point source number counts that fully cover the break flux in each energy band with small statistical errors. Due to the wide flux range of the sample, we detect breaks in the differential number counts in all energy bands and investigate what causes the different break flux in different energy bands. We also investigate the nature and the origin of the break in the differential number counts using the hardness ratio [HR = (Hc − Sc)/(Hc + Sc); see Table 1 for energy band definitions] and redshift distribution of the X-ray sources. In addition, we combine the ChaMP and CDFs (hereafter ChaMP+CDFs) number counts to cover the full available flux range. From the ChaMP and the ChaMP+CDFs number counts, we estimate the resolved CXRB flux densities in six energy bands. By adding the known unresolved CXRB (HM06) to the resolved ChaMP+CDFs CXRB flux density, we estimate the total CXRB flux densities in the 0.5–2, 1–2, and 2–8 keV bands.

In § 2, we briefly describe the ChaMP data selection. In § 3, we describe the method and results of the ChaMP simulations. In § 4, the ChaMP and the ChaMP+CDFs number counts are presented in six energy bands and are compared with previous studies. In § 5, we study the nature and origin of the break flux in the number counts. In § 6, we estimate the resolved CXRB flux densities in six energy bands and the total CXRB flux densities in three energy bands. In § 7, the summary and conclusions of this study are presented. Throughout this study, quoted errors are for a ±1 $\sigma$ confidence level, unless otherwise noted. Although we perform this study in six energy bands (see Table 1), we only present the figures in the 0.5–8, 0.5–2, and 2–8 keV bands for simplicity; however, tables include the results in all energy bands. To compare with previous studies, we assume photon indices of $\Gamma_{\rm ph}$ = 1.4 and 1.7; however, only figures with $\Gamma_{\rm ph}$ = 1.4 are provided.

## 2. THE ChaMP SAMPLE SELECTION

The X-ray point source sample is from the ChaMP X-ray point source catalog (KM07), which consists of ∼6800 X-ray sources in 149 *Chandra* archival observations. The ChaMP fields were selected to include ACIS observations at high Galactic latitude, $|b| > 20^\circ$. Fields containing large extended sources, planetary objects, fields intended by the PI for survey, and Local Group galaxies were excluded (Kim et al. 2004a). The ChaMP X-ray point source properties were obtained using a ChaMP-specific pipeline, XPIPE, which uses `wavdetect`[5] detections as source positions and extracts source properties within a given aperture appropriate for the local point-spread function (PSF) size (a 95% encircled energy radius at 1.5 keV) using `xapphot` (E. Kim et al. 2007, in preparation).

The ChaMP X-ray point source catalog is divided into main and supplementary catalogs. Thirty-five ChaMP fields overlap one another, and the supplementary catalog contains sources from the 19 shorter exposure fields among these. To avoid confusion due to duplicated fields, our analysis uses the main ChaMP catalog, which contains 130 ChaMP fields. From the main ChaMP catalog, we selected sources in the I0, I1, I2, and I3 CCD chips for 32 ACIS-I observations and sources in the I2, I3, S2, and S3 CCD chips for 98 ACIS-S observations. These sources are located within an off-axis angle of ∼15′. In addition, we selected sources with signal-to-noise ratio S/N > 1.5, corresponding to source counts of $C \gtrsim 5$. XPIPE detects sources in the B band (0.3–8 keV; see Table 1 for energy band definitions), and for all energy bands, photometry is performed at the source positions determined in the B band (see § 3 in KM07). Therefore, in our sample, it is possible to miss very soft (hard) sources that might be detected only in the soft (hard) band but not detected in the B band. For sources with S/N > 1.5 in the S (H) band, the missing percentage of very soft (hard) sources is 5% (10%), when we assume matching of all possible counterparts in the B and S (H) bands. However, since we perform simulations to correct for the incompleteness and

[5] See http://cxc.harvard.edu/ciao/.

TABLE 2
Statistical Properties of X-Ray Point Sources

| Band (1) | Number (2) | Min. (3) | Max. (4) | Median (5) | Mean (6) |
|---|---|---|---|---|---|
| | | Count[a] | | | |
| B | 5515 | 5.42 | 40535.59 | 22.57 | 69.53 |
| S | 4864 | 5.42 | 38117.52 | 19.24 | 61.50 |
| H | 2575 | 5.41 | 11604.93 | 12.73 | 28.63 |
| Bc | 5229 | 6.46 | 39760.98 | 23.46 | 70.52 |
| Sc | 4554 | 5.41 | 36010.96 | 18.24 | 57.59 |
| Hc | 3078 | 5.42 | 13624.92 | 13.72 | 31.63 |
| | | Flux[b] | | | |
| B | 5515 | 0.63 | 7175.62 | 9.09 | 25.97 |
| S | 4864 | 0.33 | 3286.49 | 4.36 | 12.78 |
| H | 2575 | 1.27 | 6690.72 | 8.61 | 21.40 |
| Bc | 5229 | 0.69 | 6767.74 | 9.04 | 25.38 |
| Sc | 4554 | 0.26 | 2395.21 | 3.21 | 9.32 |
| Hc | 3078 | 1.17 | 7112.31 | 8.87 | 21.88 |

Notes.—Col. (1): X-ray energy band (see Table 1). Col. (2): Number of sources. Col. (3): Minimum value of the sample. Col. (4): Maximum value of the sample. Col. (5): Median value of the sample. Col. (6): Mean value of the sample.
[a] Source net counts.
[b] Source flux with $\Gamma_{ph} = 1.4$ in units of $10^{-15}$ ergs cm$^{-2}$ s$^{-1}$.

bias in the ChaMP fields using the same detection technique as the ChaMP X-ray point source catalog (see § 3), these very soft (hard) sources do not introduce an additional error in our number counts.

Since the ChaMP is a *Chandra* archival survey, most ChaMP fields contain target sources selected by the PI, and those targets are likely to be biased toward special X-ray populations such as bright active galactic nuclei (AGNs). Therefore, we excluded target sources to derive less biased X-ray number counts. Our selection results in ~5500 sources in the 0.3–8 keV band from the ChaMP X-ray point source catalog. Table 2 lists the number of sources and the statistical properties of the X-ray sources in each energy band. Figure 1 shows the counts and flux distributions of the final X-ray sample. The median value of the distribution is also plotted.

## 3. THE ChaMP SIMULATIONS

To determine accurate number counts, it is necessary to correct for the incompleteness of the sample as well as for instrumental effects such as vignetting and the off-axis degradation of the PSF. There are two major techniques to correct these biases, a semi-analytical approach and a Monte Carlo simulation. The semi-analytical approach is based on the flux limit map of a given field, which contains the faintest flux corresponding to the assumed significance level of source detection (Johnson et al. 2003; Cappelluti

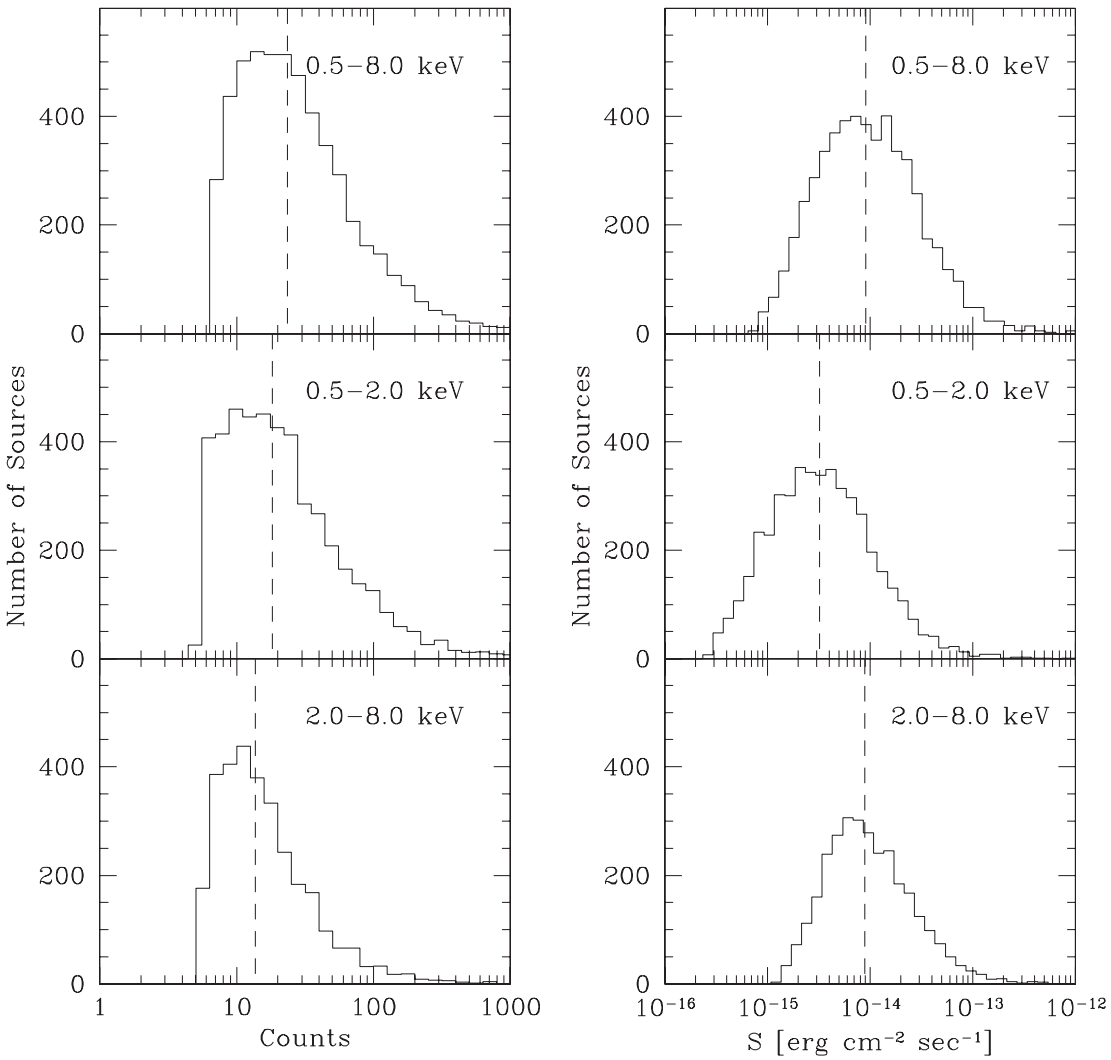


Fig. 1.—Distributions of source net counts (*left*) and flux (*right*) in three energy bands. The vertical dashed line indicates the median of the distribution. The flux was determined assuming a photon index of $\Gamma_{ph} = 1.4$.

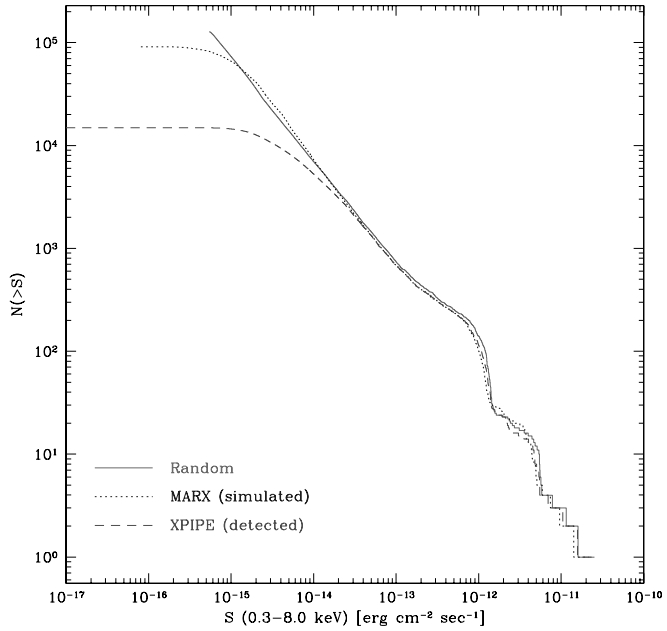


FIG. 2.—Cumulative number counts for the artificial sources in the B band. The solid line represents the number counts for sources whose fluxes were randomly selected from the assumed number counts with a slope of −1. Due to small number statistics, deviations from the assumed number counts are present in the bright flux regime. Dotted and dashed lines represent number counts for sources generated with MARX and for sources extracted with XPIPE, respectively. The effect of Eddington bias is evident at the faint fluxes ($S < 10^{-14}$ ergs cm$^{-2}$ s$^{-1}$) in the simulated source number counts. [*See the electronic edition of the Journal for a color version of this figure.*]

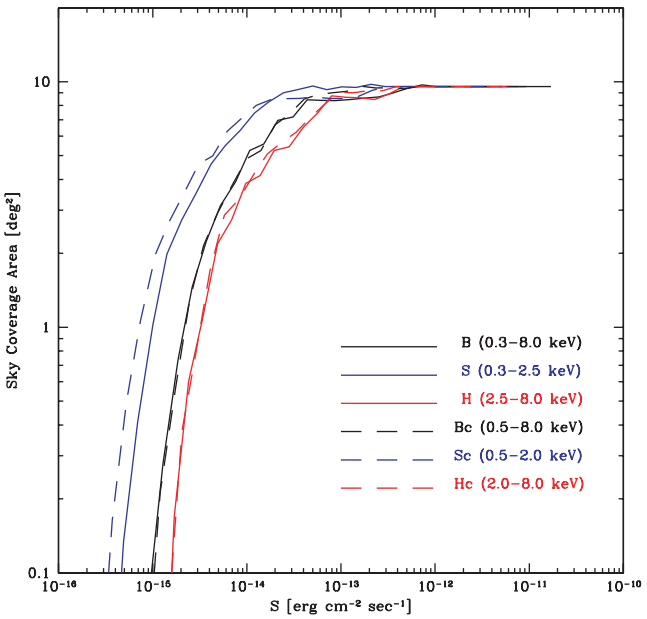


FIG. 3.—Sky coverages for sources with S/N > 1.5 in six energy bands. The full sky coverage is 9.6 deg$^2$.

et al. 2005; Chiappetti et al. 2005). This technique is efficient and reliable; however, it is possible to undercorrect the incompleteness of the field because in this method the source detection probability is a function of only the source counts. The actual source detection probability in a *Chandra* field is a complex function of off-axis angle and source counts: the detection probability decreases as off-axis angle increases and as source counts decrease (KM07). Therefore, to accurately determine the sky coverage of the ChaMP sample, we performed extensive Monte Carlo simulations to correct incompleteness and biases of the sample fields.

### 3.1. *Method*

The simulation method is described in detail in KM07 and consists of three parts, (1) generating artificial X-ray sources with MARX,[6] (2) adding them to the observed image, and (3) detecting these artificial sources with `wavdetect` and extracting source properties with `xapphot`. In step (2), we used the real *Chandra* observations to accurately reflect the effects of background counts and source confusion in the ChaMP fields.

We performed simulations using all selected observations and four CCD chips in each observation (see § 2). We generated 1000 artificial X-ray sources per sample field, which corresponds to ∼13,000 artificial X-ray sources per square degree. The number of sources in each field depends on the effective exposure time of the observation and the neutral hydrogen column density, $N_{\rm H}$, toward the observed region of the sky. On average, 11.7% of the 127,178 artificial X-ray sources are detected in our simulations, a total of 14,932 artificial X-ray sources in 130 ChaMP fields. The number of detected artificial sources is 2.5 times the ∼6000 observed sources; this number is statistically sufficient to estimate the properties of the ChaMP sample.

The form of the assumed number count distribution is not critical because we use the ratio of input to output number of sources to determine the sensitivity (Vikhlinin et al. 1995; Kim & Fabbiano 2003). The actual X-ray differential number counts are described by a broken/double power law with a faint slope of ∼−1.5 and a bright slope of ∼−2.5 (Yang et al. 2004; Basilakos et al. 2005; Chiappetti et al. 2005) in most energy bands; however, the break flux has not been well determined. Therefore, we assumed a cumulative number count distribution with a single power law with a slope of −1 corresponding to a slope of −2 in the differential number counts, taking the average of the faint and bright slopes from the literature, in the 0.3–8 keV band. From the assumed number count distribution, we randomly selected the artificial source flux. The artificial source fluxes span from $5 \times 10^{-16}$ to $5 \times 10^{-10}$ ergs cm$^{-2}$ s$^{-1}$ in the B band, covering the flux range of the observed ChaMP X-ray point sources ($6 \times 10^{-16}$ to $6 \times 10^{-12}$ ergs cm$^{-2}$ s$^{-1}$).

The spectrum of the artificial sources was assumed to be a power law ($F_\nu \propto \nu^{-\Gamma_{\rm ph}}$) with a photon index of $\Gamma_{\rm ph} = 1.7$, because the photon index $\Gamma_{\rm ph}$ for the observed ChaMP sources spans $\Gamma_{\rm ph} = 1.5$–2 (KD04; KM07). Tozzi et al. (2006) performed X-ray spectral analysis for 82 X-ray bright sources in the CDF-S and found a weighted mean value for the slope of the power-law spectrum of $\langle \Gamma_{\rm ph} \rangle \simeq 1.75 \pm 0.02$. The flux range of these bright sources in the CDF-S overlaps with the faint flux end of the ChaMP sources; therefore, we assumed that the faint ChaMP sources also have a photon index of $\Gamma_{\rm ph} \sim 1.7$. We assumed a Galactic absorption, $N_{\rm H}$ (Stark et al. 1992), for each observation; however, we did not include intrinsic absorption for the artificial source spectrum. The spectrum of each X-ray point source was generated using the XSPEC[7] package.

The artificial source's position was randomly selected in each CCD chip area, but it was rejected if the source area at a given random position had an exposure map value of less than 10% of

[6] See http://space.mit.edu/CXC/MARX/ and MARX 4.0 Technical Manual.

[7] See http://xspec.gsfc.nasa.gov.

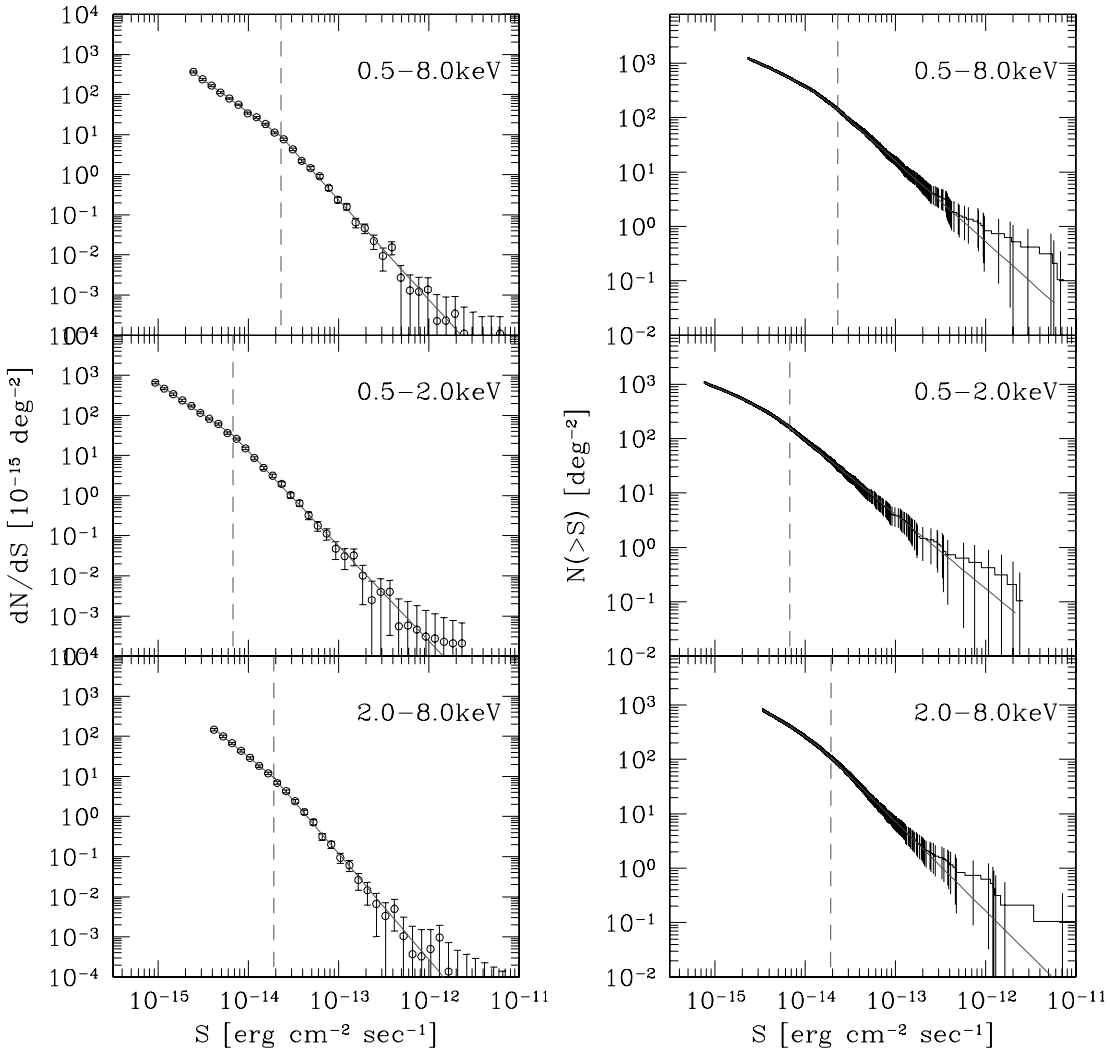


FIG. 4.— Differential (*left*) and cumulative (*right*) number counts of the ChaMP X-ray point sources in the Bc, Sc, and Hc bands (*from top to bottom, respectively*). Solid lines represent the best-fit results with a broken power law. The vertical dashed lines indicate the derived break fluxes. Source fluxes were determined assuming a photon index of $\Gamma_{ph} = 1.4$. Since we present the differential number counts brighter than a flux corresponding to 10% of the full sky coverage, the faintest bin still has sufficient sources and shows a small error bar. The error bars in the cumulative number counts are estimated by the error propagation rule using Gehrels (1986) statistics. [*See the electronic edition of the Journal for a color version of this figure.*]

the maximum. This requirement is identical to that in the ChaMP X-ray point source catalog reduction procedure. To avoid overcrowding of the artificial sources, ~250 artificial sources per CCD were divided into several groups to be added into the observed image: while we did not allow the artificial X-ray point sources to overlap one another, we allowed overlap between artificial and real X-ray sources to provide an estimate of source confusion in each observed field. This resulted in ~10 (~20) simulated images per ACIS-I (ACIS-S) CCD, corresponding ~9100 CCD images (event files) to run `wavdetect` (`xapphot`). Since ~11.7% of the artificial sources (~14,900) are detected, on average we added only ~1.6 artificial sources to each simulated image. The net counts of the overlapping artificial sources with real sources were corrected following the overlapping source correction methods described in § 3.2.2 of KM07.

### 3.2. *Sky Coverage Area*

Using the results of the simulations described in § 3.1, Figure 2 shows the number counts for artificial sources in the B band. The number count for sources whose fluxes were randomly selected from the assumed number counts (*solid line*) agree well with a slope of −1. However, there are slight statistical fluctuations at fluxes brighter than $10^{-13}$ ergs cm$^{-2}$ s$^{-1}$ due to small number statistics. The random sources were selected per observation (see § 3.1), and 1–2 bright sources out of 1000 sources result in statistical fluctuations in each observation. In addition, since we fixed the flux maximum rather than using infinitely bright flux (see § 3.1) for random sources, the cumulative number of artificial sources drops at ~$10^{-12}$ ergs cm$^{-2}$ s$^{-1}$ rather than following a line of slope −1. Since the aim of our simulations is to correct bias at faint fluxes, we do not require good statistics at bright fluxes. The number counts for artificial sources generated by MARX (*dotted line*) and that for artificial sources detected by XPIPE (*dashed line*) are also displayed. The Eddington bias, that sources with counts near the detection threshold will be preferentially detected when they have upward fluctuations (e.g., Kenter & Murray 2003), is evident at faint fluxes ($S < 10^{-14}$ ergs cm$^{-2}$ s$^{-1}$) in the simulated number counts. Near ~$10^{-14}$ ergs cm$^{-2}$ s$^{-1}$, the number of detected artificial sources starts to decrease.

Figure 3 displays sky coverage for sources with S/N > 1.5 as a function of flux in six energy bands assuming a photon index of $\Gamma_{ph} = 1.4$. The sky coverage area is the ratio of the number of detected over input sources at a given flux, multiplied by the total sky area. The full sky area is 9.6 deg$^2$. The geometrical area of a

*Chandra* CCD chip is 0.0196 deg$^2$; however, the net effective area is slightly larger due to the dither. To accurately calculate the effective area, we follow the same method as in `xapphot`: all pixels in the exposure map were summed, excluding those pixels with an exposure map value less than 10% of the maximum within the corresponding source area. This criterion automatically excludes pixel positions located near the edge of the CCD chip.

## 4. X-RAY POINT SOURCE NUMBER COUNTS

### 4.1. *The ChaMP Number Counts*

The cumulative number counts for sources brighter than a given flux $S$, corrected by the corresponding sky coverage at $S$, is

$$N(>S) = \sum_{S_i > S} \frac{1}{\Omega_i}, \tag{1}$$

where $S_i$ is the flux of the $i$th X-ray point source and $\Omega_i$ is the sky coverage that is the maximum solid angle covered by the flux $S_i$. Using the sources selected in § 2 and the corresponding sky coverage derived in § 3.2, we derived the cumulative number counts for the ChaMP point sources. Since the differential number count is a derivative form of the cumulative number count, we derived the differential number counts from the cumulative number counts resulting from equation (1) as follows:

$$\left.\frac{dN}{dS}\right|_i = -\frac{N_{i+1} - N_i}{S_{i+1} - S_i}, \tag{2}$$

where $N_i$ is the cumulative source number at flux $S_i$. Since the sky coverage rapidly decreases near the faint flux limit, there are large statistical errors for the number counts in the faint flux regime. Thus, for better statistics, we present the number counts brighter than the flux corresponding to 10% of the full sky coverage. For example, in the 0.5–8 keV band, this flux cut corresponds to $2 \times 10^{-15}$ ergs cm$^{-2}$ s$^{-1}$; 500 sources fainter than this flux are not included in the final number counts. In Figure 4, we display the ChaMP differential number counts (*left*) and cumulative number counts (*right*) in three energy bands. Statistical errors on the number counts are assigned following Gehrels (1986).

The shape of the cumulative number counts is curved rather than a single power-law feature, and the differential number counts can be fitted by a broken power law (Baldi et al. 2002; KD04) or by a double power law (Cowie et al. 2002; Harrison et al. 2003, hereafter H03; Yang et al. 2004; Chiappetti et al. 2005). Since errors for the cumulative number counts are not independent (Murdoch et al. 1973), it is difficult to estimate confidence levels of fitting parameters for the cumulative number counts. Therefore, we fitted the differential number count with a broken power law as follows:

$$\frac{dN}{dS} = \begin{cases} K(S/S_{\rm ref})^{-\gamma_1}, & S < S_b, \\ K(S_b/S_{\rm ref})^{(\gamma_2-\gamma_1)}(S/S_{\rm ref})^{-\gamma_2}, & S \geq S_b, \end{cases} \tag{3}$$

where $K$ is a normalization constant and $S_{\rm ref}$ is a normalization flux. In this study, we set a normalization flux of $S_{\rm ref} = 10^{-15}$ ergs cm$^{-2}$ s$^{-1}$. The parameter $S_b$ is the break flux at which the slope of the differential number count changes, and $\gamma_1$ and $\gamma_2$ are faint and bright power indices. The best-fit parameters for the differential number counts are listed in Table 3 for photon indices of $\Gamma_{\rm ph} = 1.4$ and 1.7. The photon index $\Gamma_{\rm ph}$ hardly affects $\gamma_1$ and $\gamma_2$, but it shifts $S_b$ somewhat. We display the best-fit results in the left panels of Figure 4. In all energy bands, we detected breaks, which appear at different fluxes in different energy bands. We discuss the break flux of the differential number count in more detail in § 5.

TABLE 3
List of the Best-Fit Parameters Excluding Target Objects

| Band (1) | $K$ (2) | $\gamma_1$ (3) | $\gamma_2$ (4) | $S_b$ (5) |
|---|---|---|---|---|
| ChaMP Data Set, $\Gamma_{\rm ph} = 1.4$ | | | | |
| S | $769 \pm 14$ | $1.57 \pm 0.01$ | $2.41 \pm 0.05$ | $9.9^{+0.7}_{-1.6}$ |
| H | $1828^{+48}_{-43}$ | $1.81 \pm 0.01$ | $2.58 \pm 0.05$ | $14.2^{+0.9}_{-1.1}$ |
| B | $1614^{+28}_{-43}$ | $1.65 \pm 0.01$ | $2.44^{+0.06}_{-0.05}$ | $25.0 \pm 1.9$ |
| Sc | $607 \pm 12$ | $1.54 \pm 0.02$ | $2.36 \pm 0.05$ | $6.8 \pm 0.5$ |
| Hc | $2040 \pm 50$ | $1.82 \pm 0.01$ | $2.65 \pm 0.07$ | $19.2^{+6.3}_{-1.8}$ |
| Bc | $1557^{+28}_{-50}$ | $1.64 \pm 0.01$ | $2.48 \pm 0.05$ | $22.9 \pm 1.6$ |
| ChaMP Data Set, $\Gamma_{\rm ph} = 1.7$ | | | | |
| S | $783 \pm 15$ | $1.58 \pm 0.01$ | $2.42 \pm 0.05$ | $10.5 \pm 0.8$ |
| H | $1774^{+44}_{-41}$ | $1.80 \pm 0.01$ | $2.58 \pm 0.05$ | $13.5 \pm 0.9$ |
| B | $1505^{+25}_{-41}$ | $1.65 \pm 0.01$ | $2.45^{+0.06}_{-0.05}$ | $21.9 \pm 1.7$ |
| Sc | $612 \pm 12$ | $1.53 \pm 0.02$ | $2.36^{+0.05}_{-0.04}$ | $6.7 \pm 0.5$ |
| Hc | $1932^{+46}_{-48}$ | $1.82 \pm 0.01$ | $2.64 \pm 0.07$ | $17.8^{+4.4}_{-1.7}$ |
| Bc | $1407^{+25}_{-48}$ | $1.64 \pm 0.01$ | $2.48 \pm 0.05$ | $19.2^{+1.3}_{-1.4}$ |
| ChaMP+CDFs Data Set, $\Gamma_{\rm ph} = 1.4$ | | | | |
| Sc | $571 \pm 11$ | $1.49 \pm 0.02$ | $2.36 \pm 0.05$ | $6.5 \pm 0.4$ |
| Hc | $1258 \pm 29$ | $1.58 \pm 0.01$ | $2.59^{+0.06}_{-0.05}$ | $14.4 \pm 0.9$ |

Notes.—Col. (1): X-ray energy band (see Table 1). Col. (2): Normalization constant. Col. (3): Faint power-law index of a broken power law. Col. (4): Bright power-law index of a broken power law. Col. (5): Break flux in units of $10^{-15}$ ergs cm$^{-2}$ s$^{-1}$.

By integrating equation (3), we can derive a formula for the cumulative number count as follows:

$$N(>S) = \int \frac{dN}{dS}\, dS', \tag{4}$$

therefore,

$$N(>S) = \begin{cases} K\left(\dfrac{1}{1-\gamma_1} - \dfrac{1}{1-\gamma_2}\right)\left(\dfrac{S_b}{S_{\rm ref}}\right)^{(1-\gamma_1)} \\ \quad + K\left(\dfrac{1}{\gamma_1 - 1}\right)\left(\dfrac{S}{S_{\rm ref}}\right)^{(1-\gamma_1)}, & S < S_b, \\ K\left(\dfrac{1}{\gamma_2 - 1}\right)\left(\dfrac{S_b}{S_{\rm ref}}\right)^{(\gamma_2-\gamma_1)}\left(\dfrac{S}{S_{\rm ref}}\right)^{(1-\gamma_2)}, & S \geq S_b, \end{cases} \tag{5}$$

where definitions of parameters are the same as in equation (3). Using the best-fit parameters derived from the differential number counts, we also plot the best-fit results for the cumulative number counts in the right panels of Figure 4.

### 4.2. *The ChaMP+CDFs Number Counts*

To measure the discrete X-ray source contributions to the CXRB, it is important to derive the number counts over a wide range of flux. So far, M03 have presented the widest flux range of number counts using a combination of three different surveys with *ROSAT*, *Chandra*, and *XMM-Newton*. Due to the different calibrations of each satellite, it is possible that additional systematic errors are

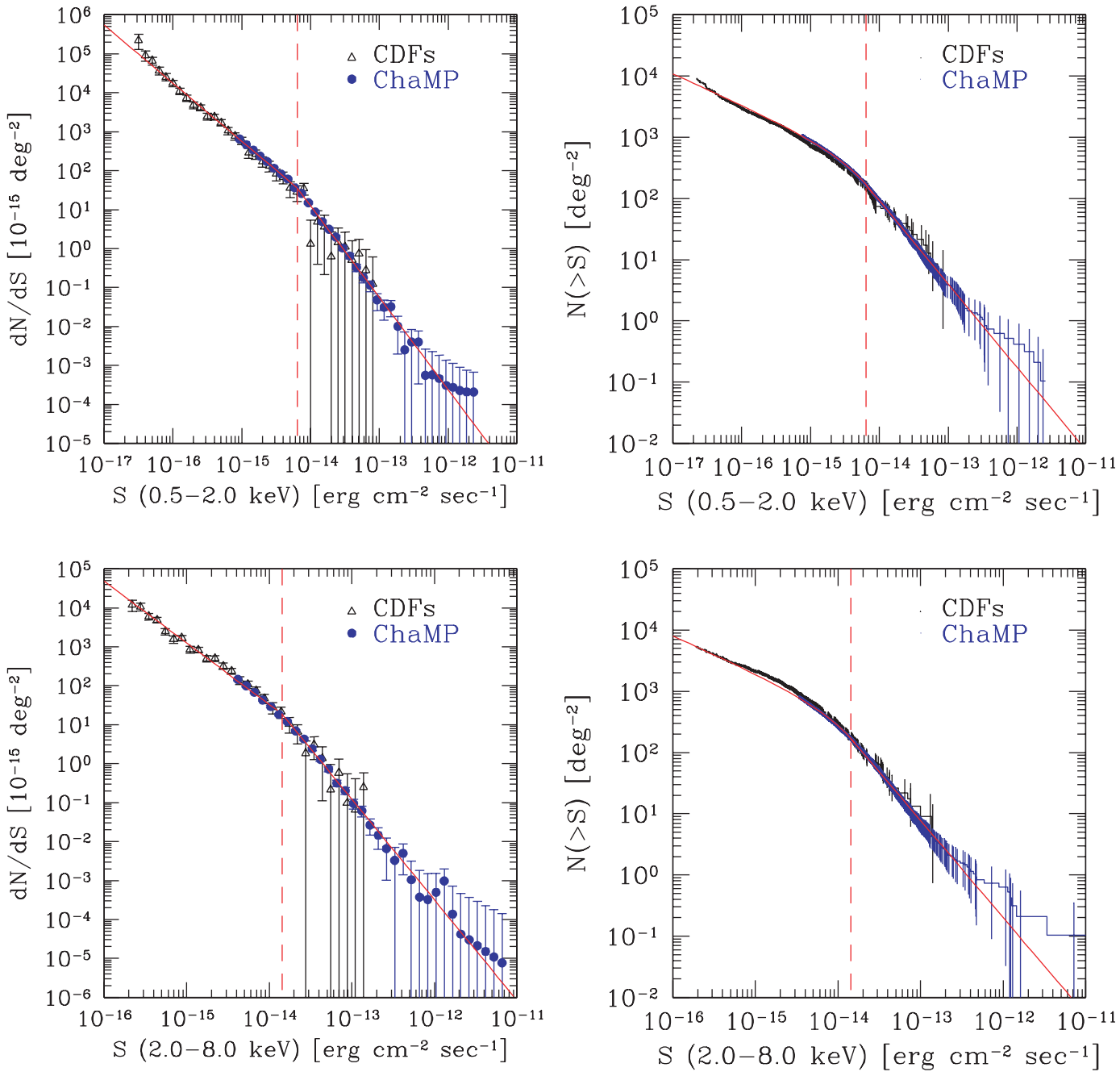


FIG. 5.— Differential (*left*) and cumulative (*right*) number counts for the ChaMP+CDFs X-ray point sources in the Sc and Hc bands. Blue filled circles and black open triangles represent the ChaMP and the CDFs data, respectively. Red lines are the best simultaneous fit results. The vertical red dashed lines indicate the derived break fluxes. Source fluxes were determined assuming a photon index of $\Gamma_{ph} = 1.4$.

introduced for this combined survey data. The ChaMP is a medium-depth survey that covers the break flux regime in each energy band but with a faint flux limit too shallow to estimate the resolved CXRB. Therefore, to cover the faint flux regime as well, we decided to use the CDFs as well as the ChaMP data to determine the number counts. Since the ChaMP and the CDFs are from the same satellite, *Chandra*, they provide number counts over a wide flux range without systematic errors due to different calibrations.

The cumulative CDF number counts (B04) are provided by the Chandra Deep Field Web site,[8] and the corresponding sky coverage is from Figure 1 of B04. Note that they combined the CDF-N and CDF-S source catalogs and then derived the CDF number counts. Using the cumulative CDF number counts and their sky coverages, we derived the differential number counts of the CDFs in the 0.5–2 and 2–8 keV bands. Then we simultaneously fitted the differential number counts of the ChaMP and the CDFs with a broken power law. In Figure 5, we display the differential and the cumulative number counts of the ChaMP+CDFs in the 0.5–2 and 2–8 keV bands. The best-fit parameters are listed in Table 3 and displayed in Figure 5 as red lines. The ChaMP+CDFs number counts cover a flux range of $2 \times 10^{-17}$ to $2.4 \times 10^{-12}$ (0.5–2 keV) and $2 \times 10^{-16}$ to $7 \times 10^{-12}$ (2–8 keV) ergs cm$^{-2}$ s$^{-1}$. The bright flux end of the ChaMP+CDFs and the faint flux end of the

[8] See http://www.astro.psu.edu/users/niel/hdf/hdf-chandra.html.

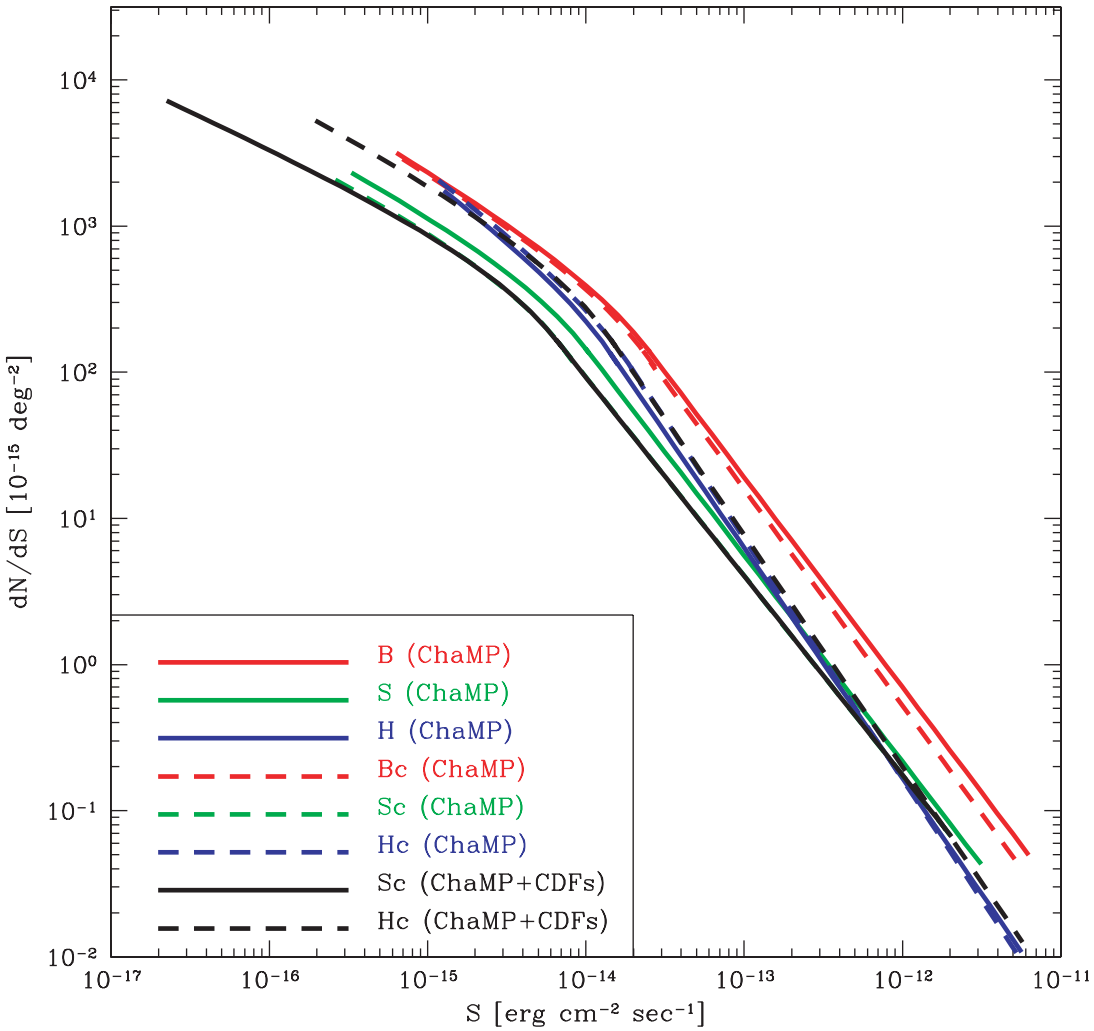


FIG. 6.— Differential number counts of the ChaMP and the ChaMP+CDFs from the best-fit results in six energy bands. Source fluxes were determined assuming a photon index of $\Gamma_{ph} = 1.4$. For energy band definitions, see Table 1.

ChaMP agree well. Thus, the number counts are well established with smaller statistical errors over a wide flux range.

Figure 6 compares the bet fits to the differential number counts of the ChaMP along with those of the ChaMP+CDFs. Overall, the ChaMP and the ChaMP+CDFs number counts agree within the uncertainties in the Sc and the Hc bands; however, in the Hc band, the faint power index $\gamma_1$ of the ChaMP ($1.83 \pm 0.16$) is steeper than that of the ChaMP+CDFs ($1.59^{+0.13}_{-0.07}$) at 1.2 $\sigma$ confidence. B04 investigated the number counts of the CDF-N and the CDF-S independently, as well as those of the combination of both CDFs, and found that in the Hc band the CDF-N is steeper than that of the CDF-S at flux fainter than $10^{-15}$ ergs cm$^{-2}$ s$^{-1}$ and that this deviation increases to 3.9 $\sigma$ at the faintest flux limits. They suggested that this is caused by field-to-field variations, as also reported by Cowie et al. (2002). Note that they did not find any significant evidence for field-to-field variations in the Hc band at fluxes brighter than $10^{-15}$ ergs cm$^{-2}$ s$^{-1}$ or across the entire flux range of the Sc band as already reported by KD04 in the ChaMP study. Although the faint flux limit of the ChaMP number counts ($\sim 2 \times 10^{-15}$ ergs cm$^{-2}$ s$^{-1}$ in the Hc band) is brighter than that of the CDFs ($\sim 2 \times 10^{-16}$), the large size of the ChaMP sample taken from 130 serendipitous *Chandra* fields provides the best estimate of the average number counts. Therefore, it is likely that the CDF-S contains fewer faint sources in the Hc band than the average number count distributions at $\gtrsim 1.2$ $\sigma$ confidence levels.

### 4.3. *Comparison with Previous Studies*

In this section, we compare the ChaMP and the ChaMP+CDFs number counts with those of previous studies. Table 4 provides the best-fit parameters, the sky coverage, the faint and bright flux limits, the fitting space (in cumulative or differential spaces), and the fitting formula for each study. Figure 7 shows the number of sources and the sky coverage of various surveys. The largest sky coverage area is 92 and 74 deg$^2$ in the soft and hard band, respectively, for the combination data of *ROSAT*, *Chandra*, and *XMM-Newton* surveys (M03). The ChaMP+CDFs covers the second largest sky area of 9.8 deg$^2$; however, it contains the largest number of sources due to the better resolution and sensitivity of *Chandra* compared with other X-ray observatories. In Figure 8, we plot the faint and bright flux limits of this and previous studies. The ChaMP covers the widest flux range in the broad band. In the soft and hard bands, M03 covers the widest flux ranges, although the ChaMP+CDFs also spans a very wide flux range. Overall, the ChaMP and the ChaMP+CDFs samples are second in sky area and flux range; however, they have the largest number of sources observed with a single satellite, *Chandra*.

TABLE 4

List of Fitting Parameters of Other Studies, ChaMP, and ChaMP+CDFs

| Data (1) | Area ($deg^2$) (2) | Band (keV) (3) | $\Gamma_{ph}$ (4) | No. (5) | $K$ (6) | $S_{ref}$ (7) | $\gamma_1$ (8) | $\gamma_2$ (9) | $S_b$ (10) | $f_{min}$ (11) | $f_{max}$ (12) | FS (13) | FM (14) | Ref. (15) |
|---|---|---|---|---|---|---|---|---|---|---|---|---|---|---|
| SSA13 | 0.03 | 0.5–2 | 1.4 | 22 | 185 | 7 | $0.7 \pm 0.2$ | ... | ... | 0.23 | 7 | C | S | 1 |
| | 0.03 | 2–10 | 1.2 | 15 | 170 | 20 | $1.05 \pm 0.35$ | ... | ... | 2.5 | 20 | C | S | 1 |
| HELLAS2XMM | 3 | 0.5–2 | 1.7 | 1022 | ... | 10 | 1.1–1.7 | $2.2^{+0.06}_{-0.09}$ | 5–6.5 | 0.59 | 500 | D | B | 2 |
| | 3 | 0.5–2 | 1.7 | 1022 | $80.8^{+6.4}_{-5.2}$ | ... | $0.93 \pm 0.05$ | ... | ... | 0.59 | 500 | C | S | 2 |
| | 3 | 2–10 | 1.7 | 495 | $229^{+29.3}_{-19.6}$ | ... | $1.34^{+0.11}_{-0.10}$ | ... | ... | 2.8 | 6000 | C | S | 2 |
| | 3 | 5–10 | 1.7 | 100 | $175.2^{+56.3}_{-36.2}$ | ... | $1.54^{+0.25}_{-0.19}$ | ... | ... | 6.2 | 1000 | C | S | 2 |
| CDFs+SSA13/SSA22 | 0.25 | 2–8 | 1.2 | 373 | $32 \pm 2$ | 10 | $1.63 \pm 0.05$ | ... | 12 | 0.2 | 100 | D | D | 3 |
| | 0.25 | ... | ... | ... | $39 \pm 5$ | 10 | ... | $2.57 \pm 0.22$ | 12 | 0.2 | 100 | D | D | 3 |
| CDF-S | 0.1 | 0.5–2 | 1.4 | 346 | $380 \pm 80$ | ... | $1.63 \pm 0.13$ | ... | ~13 | 0.06 | 50 | D | D | 4 |
| | 0.1 | 2–10 | 1.4 | 251 | $1300 \pm 100$ | ... | $1.61 \pm 0.10$ | ... | ~8 | 0.45 | 90 | D | D | 4 |
| | 0.1 | 5–10 | 1.4 | 110 | $940 \pm 100$ | ... | $1.35 \pm 0.15$ | ... | ... | 1 | 40 | C | S | 4 |
| SEXSI | 2.1 | 2–10 | 1.5 | 478 | $\sim 43.65^{+2.1}_{-2.0}$ | 10 | $1.41 \pm 0.17$ | ... | ~11 | 1 | 100 | D | D | 5 |
| | 2.1 | ... | ... | ... | $\sim 46.8 \pm 2.1$ | 10 | ... | $2.46 \pm 0.08$ | ~11 | 1 | 100 | D | D | 5 |
| ELAIS | 0.17 | 0.5–2 | 1.7 | 182 | 630 | ... | $1.72 \pm 0.09$ | ... | ... | 0.57 | 26 | D | S | 6 |
| | 0.17 | 2–8 | 1.7 | 124 | 3548 | ... | $2.07 \pm 0.15$ | ... | ... | 2.7 | 63 | D | S | 6 |
| | 0.17 | 0.5–8 | 1.7 | 225 | 1258 | ... | $1.70 \pm 0.08$ | ... | ... | 1.4 | 70 | D | S | 6 |
| BMW[a] | 91.64 | 0.5–2 | 1.4 | 4786 | $6150^{+1800}_{-1650}$ | ... | $1.82^{+0.07}_{-0.09}$ | $0.60^{+0.02}_{-0.03}$ | $14.8^{+1.27}_{-1.31}$ | 0.02 | 10000 | D | N | 7 |
| *ASCA*[b] | 73.71 | 2–10 | 1.4 | 1026 | $5300^{+2850}_{-1400}$ | ... | $1.57^{+0.10}_{-0.08}$ | $0.44^{+0.12}_{-0.13}$ | $4.5^{+3.7}_{-1.7}$ | 0.21 | 8000 | D | N | 7 |
| CDF-N+CDF-S | 0.2 | 0.5–2 | 1.4 | 724 | $3039^{+88}_{-108}$ | ... | $0.55 \pm 0.03$ | ... | ... | 0.02 | 83.73 | C | S | 8 |
| | 0.2 | 2–8 | 1.4 | 520 | $7403^{+125}_{-599}$ | ... | $0.56 \pm 0.14$ | ... | ... | 0.19 | 140.80 | C | S | 8 |
| CLASXS | 0.4 | 0.5–2 | 1.4 | 310 | $12.49 \pm 0.02$ | ... | $1.7 \pm 0.2$ | ... | ~10 | 0.5 | 35 | D | D | 9 |
| | 0.4 | 0.5–2 | 1.4 | 310 | 78.81 | ... | ... | 2.5 (fixed) | ~10 | 0.5 | 35 | D | D | 9 |
| | 0.4 | 2–8 | 1.4 | 235 | $38.1 \pm 0.2$ | ... | $1.65 \pm 0.4$ | ... | 10–30 | 3 | 90 | D | D | 9 |
| | 0.4 | 2–8 | 1.4 | 235 | $45.60 \pm 0.5$ | ... | ... | $2.4 \pm 0.6$ | 10–30 | 3 | 90 | D | D | 9 |
| *XMM-Newton*/2dF | 2 | 0.5–2 | ... | 432 | ... | ... | ... | ... | ... | 2.7 | ~500 | ... | ... | 10 |
| | 2 | 0.5–8 | ... | 462 | ... | ... | $1.8 \pm 0.2$ | ... | ~60 | 6.0 | ~700 | D | D | 10 |
| | 2 | ... | ... | ... | ... | ... | ... | $2.3 \pm 0.1$ | ~60 | 6.0 | ~700 | D | D | 10 |
| *XMM-Newton* LSS | 3.4 | 0.5–2 | 1.7 | 1028 | 384.2 | 1 | $1.42^{+0.14}_{-0.15}$ | ... | $10.6^{+3.0}_{-2.2}$ | ~1 | 700 | D | D | 11 |
| | 3.4 | 0.5–2 | 1.7 | 1028 | 6515 | 1 | ... | $2.62^{+0.25}_{-0.22}$ | $10.6^{+3.0}_{-2.2}$ | ~1 | 700 | D | D | 11 |
| | 3.4 | 2–10 | 1.7 | 328 | ... | 1 | $1.53^{+0.51}_{-1.16}$ | ... | $21.4^{+8.1}_{-5.4}$ | ~7 | 500 | D | D | 11 |
| | 3.4 | 2–10 | 1.7 | 328 | $4.5 \times 10^4$ | 1 | ... | $2.91^{+0.45}_{-0.30}$ | $21.4^{+8.1}_{-5.4}$ | ~7 | 500 | D | D | 11 |
| ChaMP | 1.1 | 0.5–2 | 1.7 | 707 | $2030 \pm 210$ | 1 | $1.40 \pm 0.30$ | $2.2 \pm 0.20$ | $6 \pm 2$ | 0.6 | 100 | D | B | 12 |
| | 1.1 | 2–8 | 1.4 | 236 | $3160 \pm 250$ | ... | ... | $2.10 \pm 0.10$ | ... | 4 | 400 | C | S | 12 |
| | 9.6 | 0.5–2 | 1.4 | 4554 | $607 \pm 12$ | 1 | $1.54 \pm 0.02$ | $2.36 \pm 0.05$ | $6.8 \pm 0.5$ | 0.26 | 2395.21 | D | B | 13 |
| | 9.6 | 2–8 | 1.4 | 3078 | $2040 \pm 50$ | 1 | $1.82 \pm 0.01$ | $2.65 \pm 0.07$ | $19.2^{+6.3}_{-1.8}$ | 1.17 | 7112.31 | D | B | 13 |
| | 9.6 | 0.5–8 | 1.4 | 5229 | $1557^{+28}_{-50}$ | 1 | $1.64 \pm 0.01$ | $2.48 \pm 0.05$ | $22.9 \pm 1.6$ | 0.69 | 6767.74 | D | B | 13 |
| | 9.6 | 0.3–2.5 | 1.4 | 4864 | $769 \pm 14$ | 1 | $1.57 \pm 0.01$ | $2.41 \pm 0.05$ | $9.9^{+0.7}_{-1.6}$ | 0.33 | 3286.49 | D | B | 13 |
| | 9.6 | 2.5–8 | 1.4 | 2575 | $1828^{+48}_{-43}$ | 1 | $1.81 \pm 0.01$ | $2.58 \pm 0.05$ | $14.2^{+0.9}_{-1.1}$ | 1.27 | 6690.72 | D | B | 13 |
| | 9.6 | 0.3–8 | 1.4 | 5515 | $1614^{+28}_{-43}$ | 1 | $1.65 \pm 0.01$ | $2.44^{+0.06}_{-0.05}$ | $25.0 \pm 1.9$ | 0.63 | 7175.62 | D | B | 13 |
| ChaMP+CDFs | 9.8 | 0.5–2 | 1.4 | 4554 + 724 | $571 \pm 11$ | 1 | $1.49 \pm 0.02$ | $2.36 \pm 0.05$ | $6.5 \pm 0.4$ | 0.02 | 2395.21 | D | B | 13 |
| | 9.8 | 2–8 | 1.4 | 3078 + 520 | $1258 \pm 29$ | 1 | $1.58 \pm 0.01$ | $2.59^{+0.06}_{-0.05}$ | $14.4 \pm 0.9$ | 0.19 | 7112.31 | D | B | 13 |

Notes.—Col. (1): Data used. Col. (2): Sky coverage of the sample. Col. (3): X-ray energy band. Col. (4): Assumed photon index. Col. (5): Number of sources in the sample. Col. (6): Normalization constant. Col. (7): Normalization flux in units of $10^{-15}$ ergs $cm^{-2}$ $s^{-1}$. Col. (8): Faint power-law index. Col. (9): Bright power-law index. Col. (10): Break flux in units of $10^{-15}$ ergs $cm^{-2}$ $s^{-1}$. Col. (11): Faint flux limit of the sample in units of $10^{-15}$ ergs $cm^{-2}$ $s^{-1}$. Col. (12): Bright flux limit of the sample in units of $10^{-15}$ ergs $cm^{-2}$ $s^{-1}$. Col. (13): Fitting domain (C: cumulative number count; D: differential number count). Col. (14): Fitting formula (S: single power law; B: broken power law; D: double power law; N: nonlinear formula); see eq. [6] in text. Col. (15): Reference.

[a] BMW (Brera Multiscale Wavelet)–HRI (High Resolution Imager), HELLAS2XMM, BMW–CDF-S, and BMW–HDF (Hubble Deep Field).

[b] *ASCA*–HSS (Hard Serendipitous Survey), HELLAS2XMM, BMW–CDFS, and BMW–HDF.

References.—(1) Mushotzky et al. 2000; (2) Baldi et al. 2002; (3) Cowie et al. 2002; (4) Rosati et al. 2002; (5) H03; (6) Manners et al. 2003; (7) M03; (8) B04; (9) Yang et al. 2004; (10) Basilakos et al. 2005; (11) Chiappetti et al. 2005; (12) KD04; (13) this study.

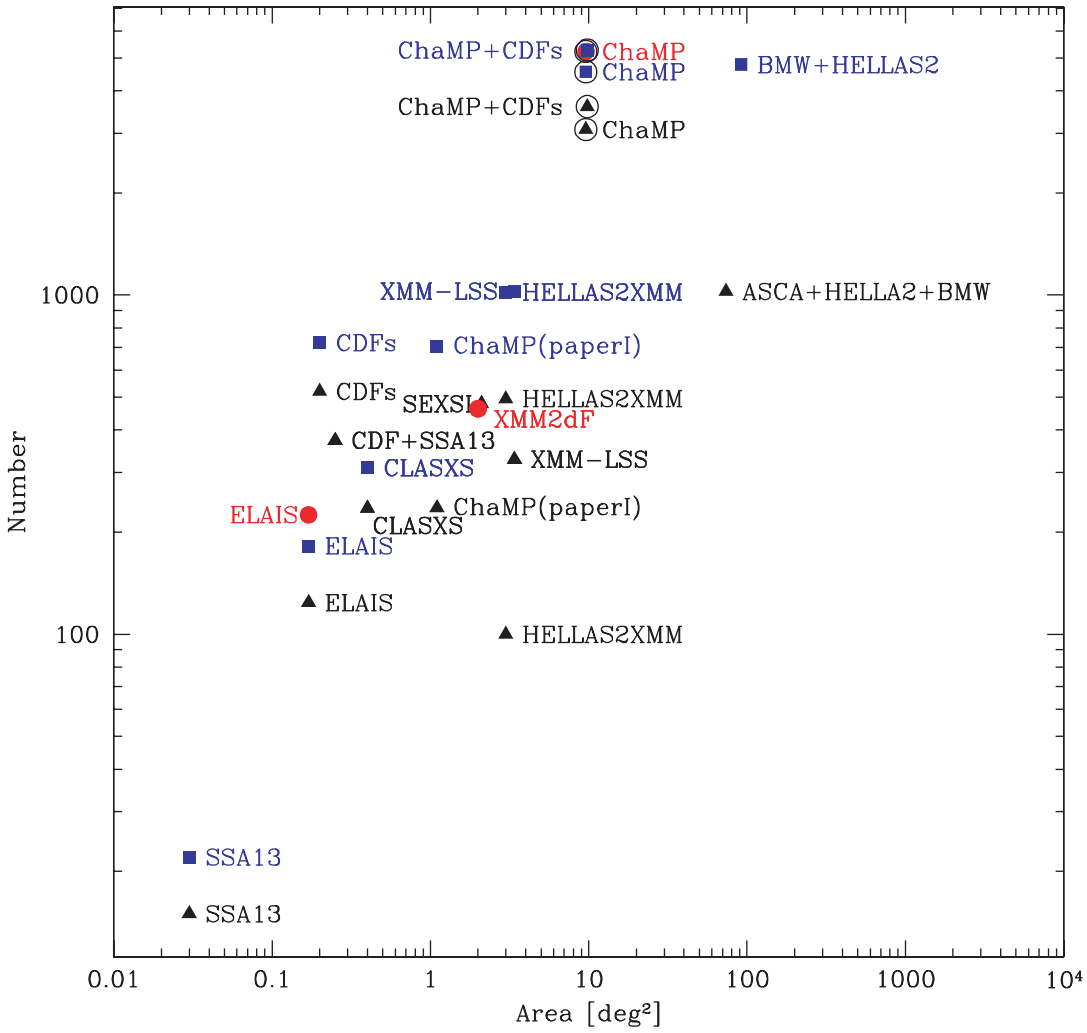


FIG. 7.—Number of sources and covered sky areas for various studies. Red circles, blue squares, and black triangles represent the broad, soft, and hard energy bands, respectively. References and parameters are listed in Table 4. The ChaMP contains ~5200 sources in the 0.5–8 keV band and covers 9.6 deg$^2$ in sky area, and the ChaMP+CDFs covers 9.8 deg$^2$. For this study, the 0.5–2, 2–8, and 0.5–8 keV bands are used and are marked with open circles for clear comparison.

The differential number counts can be described by a double power law (Cowie et al. 2002; H03; Yang et al. 2004; Basilakos et al. 2005; Chiappetti et al. 2005) or by a broken power law (Baldi et al. 2002; KD04). Manners et al. (2003) fitted their differential number counts with a single power law. M03 introduced a fitting formula for the cumulative number counts, which is a combination of two power laws (see eq. [2] in M03), and they fitted their number counts in differential space as follows:

$$\frac{dN}{dS} = K\left(2\times10^{-15}\right)^{\gamma_1}\left[\frac{\gamma_1 S^{(\gamma_1-1)} + \gamma_2 S_b^{(\gamma_1-\gamma_2)} S^{(\gamma_2-1)}}{\left(S^{\gamma_1} + S_b^{(\gamma_1-\gamma_2)} S^{\gamma_2}\right)^2}\right], \quad (6)$$

where $\gamma_1$ and $\gamma_1$ are the two power indices, $K$ is a normalization factor, and $S_b$ is the discontinuity in the cumulative number count space. Therefore, we cannot directly compare the exact parameters of equation (6) with those of a double power law or a broken power law.

In Figure 9, we compare the double or broken power-law slopes of the differential number counts for this study with those for previous studies in the soft (*left*) and the hard (*right*) bands, respectively. In both soft and hard bands, the slopes at faint ($\gamma_1$) and at bright ($\gamma_2$) fluxes for the ChaMP+CDFs agree with those of previous studies within the uncertainties. We note that $\gamma_2$ of the ChaMP+CDFs is slightly steeper than that for the previous ChaMP study (KD04), in which the hard band number count was fitted by single power law only for the bright flux regime due to the shallow faint flux limit. In this study, in the hard band, the $\gamma_1$ for the ChaMP is slightly steeper than that for Cowie et al. (2002), H03, and the ChaMP+CDFs. Overall, the ChaMP+CDFs number counts agree with those of previous studies within the uncertainties in the soft and hard bands, and they present statistically robust number counts with the smallest uncertainties.

## 5. BREAK OF THE DIFFERENTIAL NUMBER COUNTS

### 5.1. *Origin of Different Break Fluxes in Different Bands*

In § 4, we detected the break fluxes of the differential number counts in six energy bands, which have different flux levels in each energy band (see col. [5] in Table 3). The simplest explanation is that the break flux shifts as a function of energy band due to the corresponding flux levels in each band. To investigate this possibility, we estimate the flux shift by rescaling the break flux in a given energy band into the other energy bands using an assumed X-ray source spectrum. We assumed a single power-law model for the spectra for the X-ray sources and estimated the

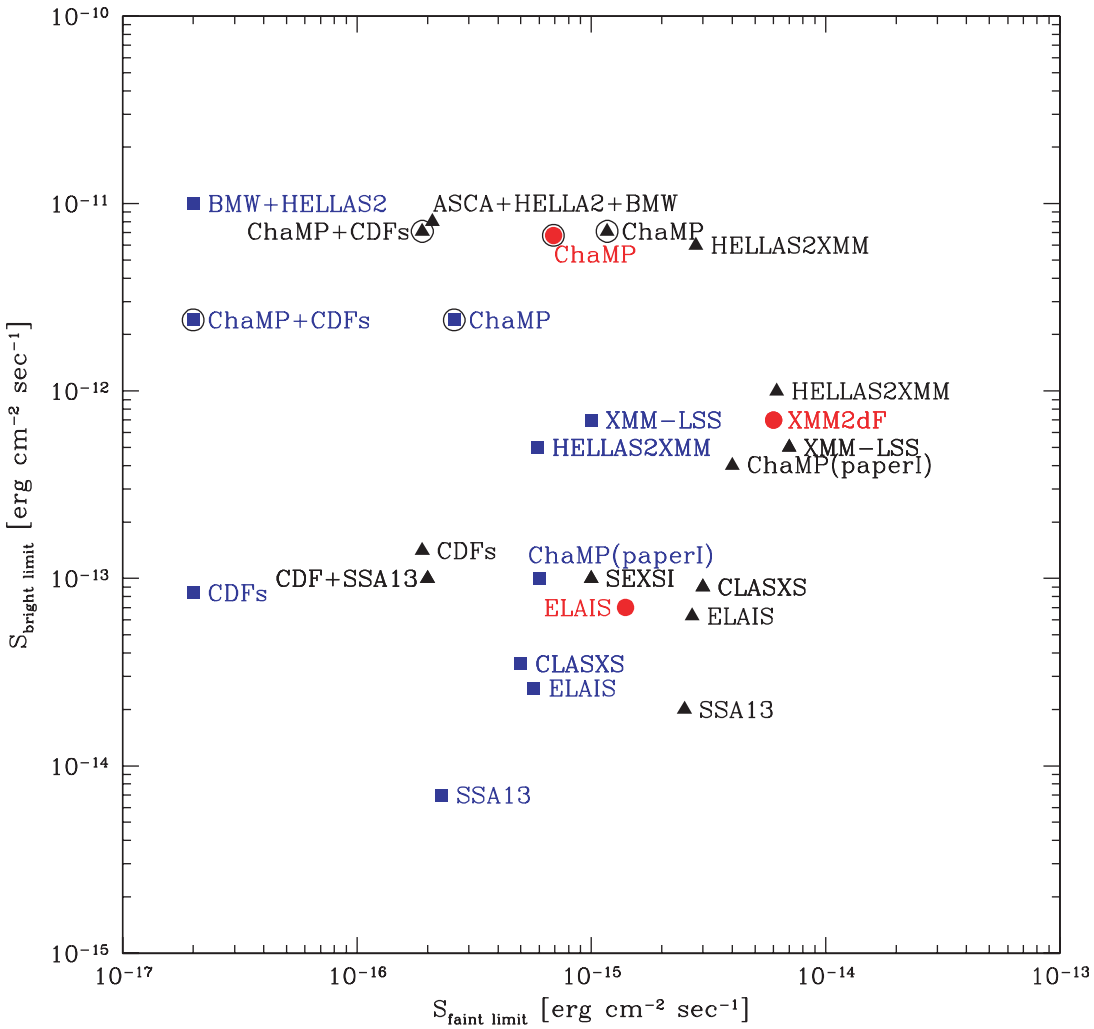


FIG. 8.—Faint and bright flux limits of various studies. Red circles, blue squares, and black triangles represent the broad, soft, and hard energy bands, respectively. References and parameters are listed in Table 4. For this study, the 0.5–2, 2–8, and 0.5–8 keV bands are used and are marked with open circles for clear comparison. We note that the faint and bright flux limits of the ChaMP are estimated from ChaMP sources with S/N $>$ 1.5. For the other studies, the faint and bright flux limits are from the literature or from our own visual estimations based on their number counts.

expected break fluxes $S_{b,\rm exp}$ in each energy band relative to a given break flux $S_{b,\rm std}$ in a standard band as follows:

$$S_{b,\rm exp}(E_1 - E_2) = S_{b,\rm std} \frac{\int_{E_1}^{E_2} E^{-\Gamma_{\rm ph}} E\, dE}{\int_{E_{S1}}^{E_{S2}} E^{-\Gamma_{\rm ph}} E\, dE}, \qquad (7)$$

where $S_{b,\rm std}$ is a break flux in a standard $E_{S1} - E_{S2}$ keV energy band and $\Gamma_{\rm ph}$ is the photon index of a spectrum. To calculate the expected break fluxes of the ChaMP and the ChaMP+CDFs, we used $S_{b,\rm std} = 2.5 \times 10^{-14}$ and $2.2 \times 10^{-14}$ ergs cm$^{-2}$ s$^{-1}$, which are the measured break fluxes in the 0.3–8 keV band with a photon index of $\Gamma_{\rm ph} = 1.4$ and 1.7, respectively.

In Figure 10, we compare the expected and measured break fluxes of the ChaMP, ChaMP+CDFs, and *XMM-Newton* LSS (Chiappetti et al. 2005) number counts in several X-ray energy bands. For the *XMM-Newton* LSS, the expected break flux is calculated by assuming a photon index of $\Gamma_{\rm ph} = 1.7$, and $S_{b,\rm std}$ is the measured break flux in the He (2–10 keV) band for consistency with their study. Overall, expected and measured break fluxes agree within the uncertainties. Since M03 fitted their differential number counts with a nonlinear equation (see eq. [6]) rather than a broken or a double power law, we cannot include their results. However, according to our own visual estimations, the break fluxes of their study also follow the trend in Figure 10. Therefore, we conclude that the break flux shifts as a function of energy band due to the corresponding flux levels in each band. Although we cannot rule it out without detailed source classification, which is beyond the scope of this paper, there is no need to invoke a different population to explain the shift.

### 5.2. *Cause of the Break*

In § 5.1, we found that different break flux levels in different energy bands could be explained by the identical X-ray population(s) in each energy band. Then what causes the break flux? To answer this question, it is best to classify all X-ray sources using optical spectroscopy and then to investigate which population(s) is responsible for a break in their number counts. However, it is difficult to obtain optical spectra of X-ray sources: some X-ray sources have very faint or no optical counterparts. B04 classified their CDF sources based on X-ray–to–optical flux ratio, optical spectrum, and X-ray properties such as X-ray spectrum and luminosity, and determined the number counts for X-ray populations such as AGNs, star-forming galaxies, and Galactic stars. They classified AGNs in more detail, such as type 1, type 2, unobscured, and obscured AGNs, and they determined the number counts for

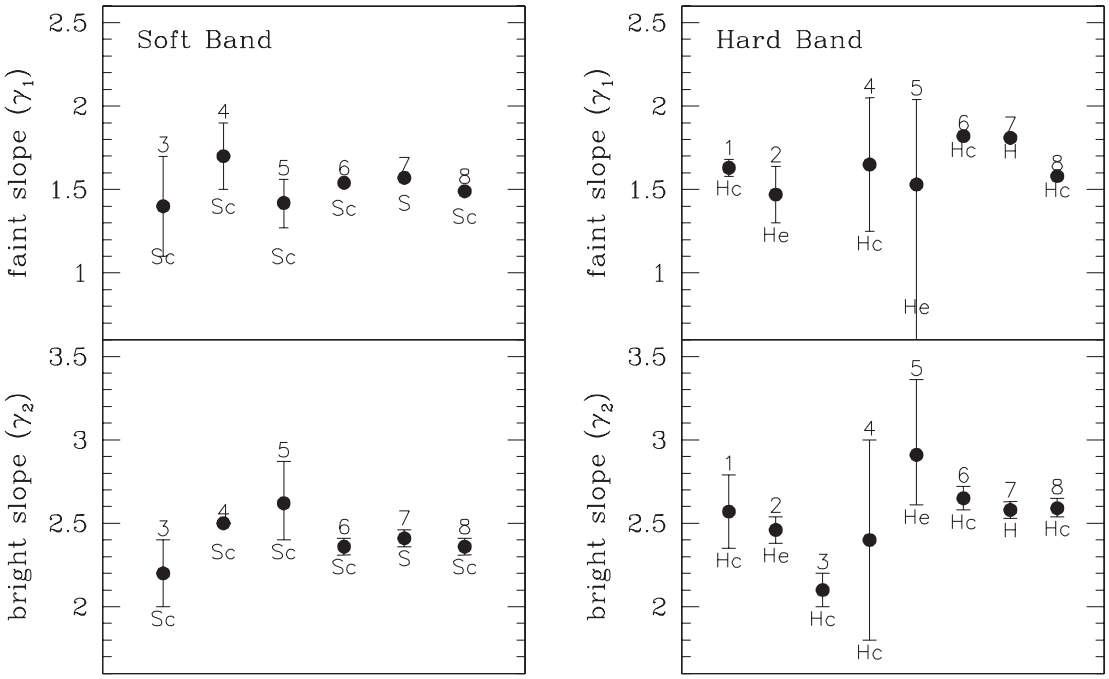


FIG. 9.—Faint (*top*) and bright (*bottom*) power indices of the differential number counts for this and previous studies in the soft (*left*) and the hard (*right*) bands. The references are as follows: (1) Cowie et al. (2002); (2) H03; (3) KD04; (4) Yang et al. (2004); (5) Chiappetti et al. (2005); (6–7) this study for the ChaMP; (8) this study for the ChaMP+CDF. The energy bands of each study are also marked here; for their definitions, see Table 1. Note that Yang et al. (2004) fixed the bright slope as 2.5 in the Sc band having no error.

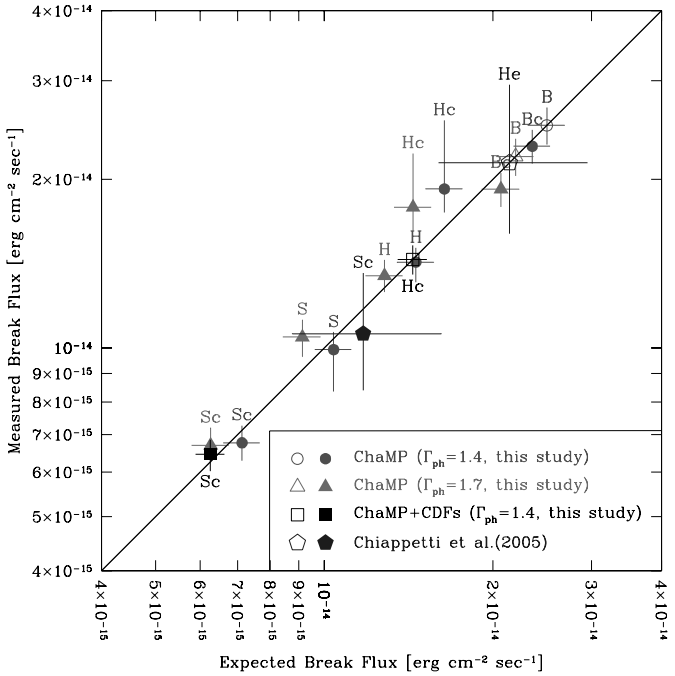


FIG. 10.—Comparison of the expected and the measured break fluxes of the differential number counts in various energy bands. Assuming a single power-law model for the X-ray spectrum, the expected break flux in each band (*filled symbols*) was calculated by converting the $S_{b,\mathrm{std}}$ (see eq. [7]), which is the measured break flux in the B (ChaMP, *open circle and open triangle*), Hc (ChaMP+CDFs, *open square*), or He (Chiappetti et al. 2005, *open pentagon*) band. For the ChaMP, photon indices of $\Gamma_{\mathrm{ph}} = 1.4$ (*circles*) and $\Gamma_{\mathrm{ph}} = 1.7$ (*triangles*) were assumed. A photon index of $\Gamma_{\mathrm{ph}} = 1.7$ is assumed for Chiappetti et al. (2005) for self-consistency with their study. The solid line represents the line of equality for expected and measured break fluxes and is shown for illustrative comparison. The energy bands are listed in Table 1. [*See the electronic edition of the Journal for a color version of this figure*.]

each AGN subclass. However, the flux limits of the CDFs are not bright enough to investigate the origin of break fluxes.

The ChaMP is a multiwavelength survey, including follow-up at optical, spectroscopic, IR, and radio wavelengths, as well as matching with published catalogs such as SDSS (Sloan Digital Sky Survey) and 2MASS (Two Micron All Sky Survey). Since these follow-up surveys are not yet completed, only part of the ChaMP sample can be classified on the basis of multiwavelength properties. The follow-up surveys of the ChaMP are still ongoing, and we will be able to investigate this issue in more detail with source classifications, covering break flux regimes. Thus, in this study we use only the X-ray properties such as the hardness ratio [HR = (Hc − Sc)/(Hc + Sc)] to investigate the cause of the break flux and include all ChaMP X-ray sources. The HR of the ChaMP sources was calculated using a Bayesian approach that models the detected counts as a Poisson distribution rather than a Gaussian distribution to successfully describe the statistical nature of the faint sources (Park et al. 2006; KM07).

#### 5.2.1. *Hardness Ratio and Break Flux*

H03 constructed the differential number counts for the Serendipitous Extragalactic X-ray Source Identification (SEXSI) sources in the 2–10 keV band divided into hard and soft sources at a hardness ratio of HR = 0. They found that the number counts for the soft (HR < 0) sources show a break while those for the hard (HR > 0) sources do not. They suggested that, on average, the hard sources may be at lower redshift, so they do not show the cosmological evolutionary effects that cause the break. Following H03, we investigated the HR dependence of the break flux for the ChaMP number counts in all energy bands.

The left panels of Figure 11 show HR distributions of the ChaMP sources as a function of flux in three energy bands. The break fluxes ($S_b$) reported in Table 3 of § 4 are also plotted. In the right panels of Figure 11, we display the number distributions of the HR for sources in the following categories: all sources, sources fainter than the break flux ($S < S_b$), and sources brighter

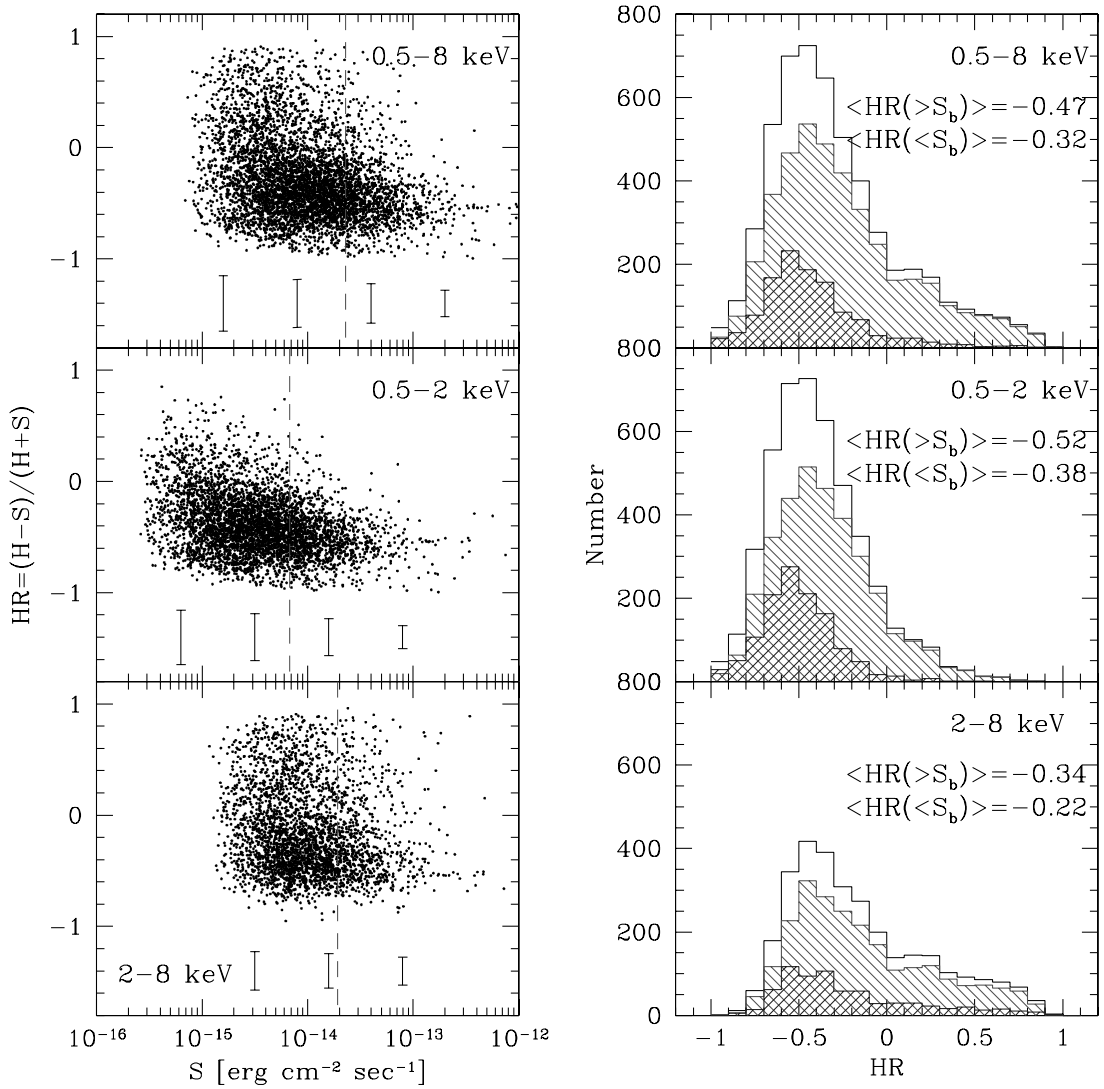


FIG. 11.—*Left*: Hardness ratio (HR) distributions as a function of flux in three energy bands. A photon index of $\Gamma_{ph} = 1.4$ was assumed. Error bars plotted at the bottom of each panel are the typical uncertainties of the hardness ratio at several flux bins. The vertical dashed line indicates the break flux ($S_b$ in Table 3) in each energy band. *Right*: Hardness ratio distributions in the following flux ranges: entire flux range (*open histogram*), $S < S_b$ (*gray hatched histogram*), and $S > S_b$ (*black hatched histogram*). The median hardness ratio of the faint and bright samples are marked in each panel. [*See the electronic edition of the Journal for a color version of this figure*.]

than the break flux ($S > S_b$). In all energy bands, there are fewer hard than soft sources at bright fluxes. We performed a Kolmogorov-Smirnov test (KS test; Press et al. 1992) to estimate the probability of faint and bright samples having the same hardness ratio distribution, and it is significantly low (prob $< 1 \times 10^{-10}$) in each energy band. Overall, most hard sources are distributed at $S < S_b$, while soft sources cover the entire flux range. Thus, we defined samples at HR $\lesssim 0$ in all energy bands to investigate the relation between the source HR and the break in the number counts. In § 5.2.3, we investigate the flux-hardness ratio ($S$-HR) diagram in more detail by performing a simple simulation for a test X-ray source over a range of redshift and absorption to understand why bright, hard sources are rare in all energy bands.

In the left panels of Figure 12, we display the differential number counts for the soft (HR $< 0$) and the hard (HR $> 0$) sources in three energy bands. We fitted the soft sources with a broken power law and the hard sources with a single power law. The best-fit parameters are listed in Table 5 and displayed in Figure 12 as solid lines. In all energy bands, the differential number counts for soft sources show a break while those for hard sources do not. We performed a KS test (Press et al. 1992) for the flux distribution of the soft and hard sources, and there is no possibility that those samples have the same flux distribution (prob $< 4 \times 10^{-17}$) in each energy band. To statistically confirm the absence of the break in the hard source number counts, we also performed an $F$-test, which is a model comparison test to select the best model from two competing models, a single and a broken power law. We used the `ftest` in the Sherpa[9] tool, and a standard criterion of `ftest` for selecting the complex model is significance $< 0.05$ (the 95% criterion of statistics). We fitted the hard source number counts with both a single and a broken power law, and the broken power-law model was rejected (significance $> 6 \times 10^{-2}$) in all energy bands. We note that for the soft source number counts, the single power-law model was rejected (significance $< 5 \times 10^{-3}$) in all energy bands.

We note that the number of soft sources is larger than that of hard sources by a factor of $\sim$10 ($\sim$2) in the Sc (Hc) band (see Table 5); thus, it is possible that the hard sources do not show the break due to small number statistics. To check this possibility, we produced 1000 random subsets from the soft sources in each

[9] See http://asc.harvard.edu/sherpa/threads/index.html.

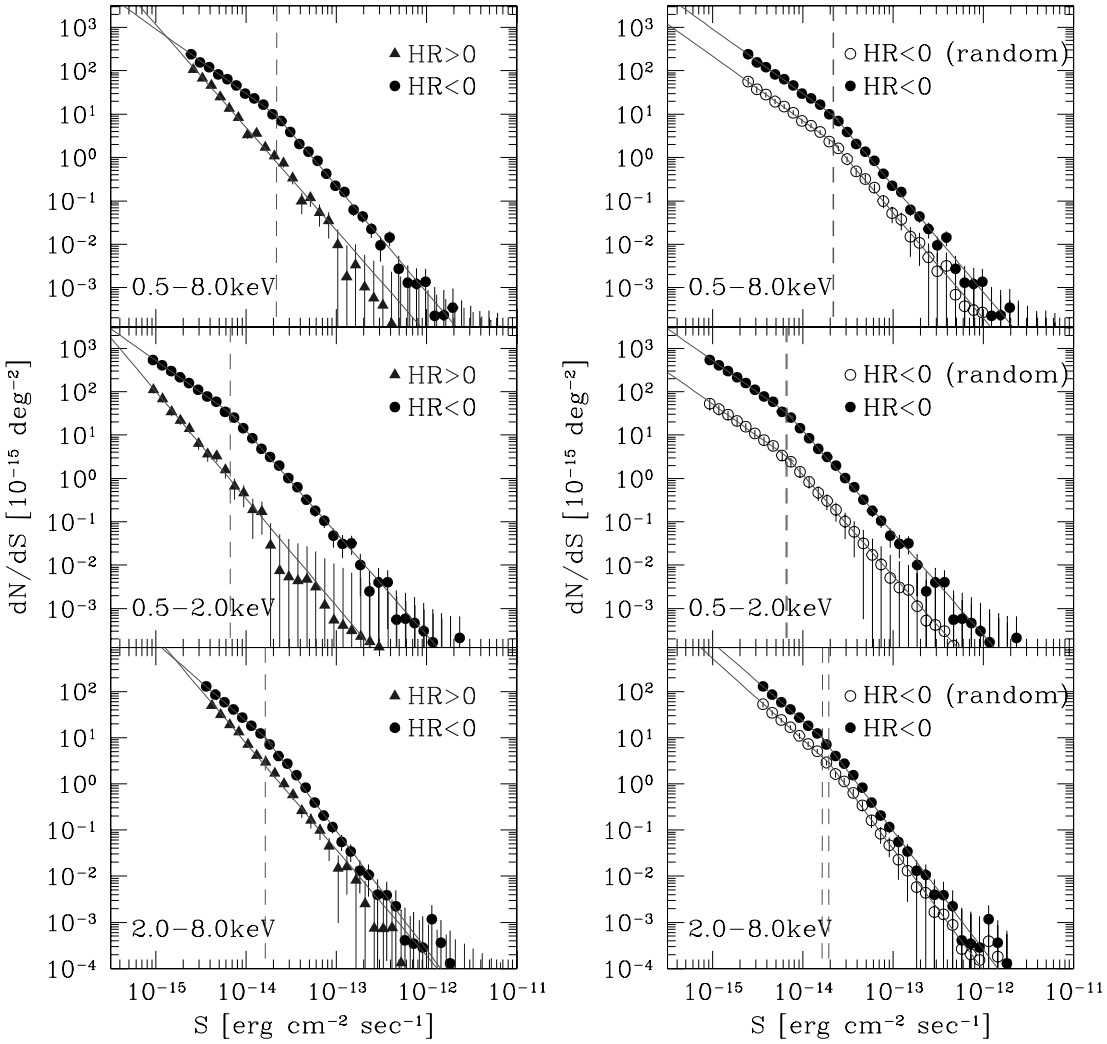


FIG. 12.—*Left*: Differential number counts for the soft (HR $< 0$, *black circles*) and hard (HR $> 0$, *gray triangles*) sources in three energy bands. Soft sources show a break and are fitted with a broken power law, while hard sources do not show a break and are fitted with a single power law. Solid lines are the best-fit results (see Table 5). The vertical dashed line is the break flux in the soft source number counts. *Right*: Averaged differential number counts from 1000 random subsets of soft sources (*open circles*). Each subset has the same number of soft sources as hard sources. Even with the reduced statistics, soft sources still show a significant break and are fitted with a broken power law. The number counts for all soft sources ( *filled circles*) is plotted in each energy band for comparison. [*See the electronic edition of the Journal for a color version of this figure*.]

energy band: each subset has the same number of sources as the hard source samples. We derived the differential number counts for each subset and display their averaged differential number counts in the right panels of Figure 12. The error bar represents the averaged error from each differential number count. We note that the statistical fluctuation for each random subset is comparable to the averaged error. Even with the reduced statistics, soft sources still show a detectable break. Thus, the smaller number of hard sources does not prevent detection of a break in our sample. Our results agree with those reported by H03 in the 2–10 keV band. Therefore, we conclude that the soft sources are responsible for the break in the differential number counts in all energy bands.

We compare the best-fit parameters of the soft and the hard subsamples with those of the total sample, which includes all sources regardless of HR (see § 4 and Table 3). In Figures 13*a*–13*c*, we compare the soft sample with the total sample: the faint power-law indices are systematically shallower (at 5.7 $\sigma$) than those of the total samples, while the bright power-law indices and break fluxes agree well with those of the total samples, within the uncertainties. In Figure 13*d*, we compare the hard sample with the total sample: the hard band (H and Hc) indices are shallower (at 2.6 $\sigma$) than those of the total samples, while the broad and soft band indices agree to within the uncertainties. To quantitatively estimate the slope changes that indicate the strength of the break, we introduce a break factor as follows:

$$\mathrm{BF} \equiv \frac{\gamma_2 - \gamma_1}{\gamma_2 + \gamma_1}, \tag{8}$$

where $\gamma_1$ and $\gamma_2$ are the faint and bright power indices of the differential number count (see eq. [3]). As the strength of the break increases, the break factor increases. The break factors of the total and the soft sample are listed in Table 6. We found that the break factors tend to be smaller in the total samples than in soft samples for all energy bands and that the break factors tend to be larger in the soft bands than in the hard bands.

#### 5.2.2. *Redshift Distributions of Soft and Hard Sources*

Why do soft sources show a break while hard sources do not? H03 suggested that the hard sources may be predominantly at lower redshifts and thus do not show the cosmological evolution effects that cause the break. To investigate this suggestion, we

TABLE 5
List of the Best-Fit Parameters of the Soft and Hard Sources

| | Soft Source (HR < 0) | | | | | Hard Source (HR > 0) | | |
|---|---|---|---|---|---|---|---|---|
| Band (1) | No. (2) | $K$ (3) | $\gamma_1$ (4) | $\gamma_2$ (5) | $S_b$ (6) | No. (7) | $K$ (8) | $\gamma$ (9) |
| | | | | $\Gamma_{ph} = 1.4$ | | | | |
| S | 4289 | $580 \pm 12$ | $1.43 \pm 0.02$ | $2.35 \pm 0.04$ | $8.5 \pm 0.5$ | 575 | $217^{+22}_{-20}$ | $2.45^{+0.08}_{-0.07}$ |
| H | 1787 | $896 \pm 31$ | $1.63 \pm 0.02$ | $2.58^{+0.08}_{-0.07}$ | $13.5^{+1.1}_{-1.3}$ | 787 | $1614^{+209}_{-184}$ | $2.35 \pm 0.05$ |
| B | 4427 | $900^{+18}_{-31}$ | $1.46 \pm 0.01$ | $2.35 \pm 0.04$ | $20.6^{+1.4}_{-1.3}$ | 1088 | $1195^{+106}_{-98}$ | $2.34 \pm 0.04$ |
| Sc | 4149 | $521 \pm 11$ | $1.47 \pm 0.02$ | $2.35 \pm 0.05$ | $6.7^{+0.5}_{-0.4}$ | 405 | $101^{+11}_{-10}$ | $2.47 \pm 0.10$ |
| Hc | 2185 | $1129 \pm 33$ | $1.69 \pm 0.01$ | $2.57 \pm 0.07$ | $16.4^{+4.4}_{-1.5}$ | 893 | $1509^{+182}_{-163}$ | $2.30^{+0.05}_{-0.04}$ |
| Bc | 4235 | $916^{+18}_{-33}$ | $1.49 \pm 0.01$ | $2.45 \pm 0.05$ | $21.8 \pm 1.4$ | 994 | $1160^{+116}_{-105}$ | $2.37^{+0.05}_{-0.04}$ |
| | | | | $\Gamma_{ph} = 1.7$ | | | | |
| S | 4289 | $588 \pm 12$ | $1.44 \pm 0.02$ | $2.34 \pm 0.04$ | $8.7^{+0.6}_{-0.5}$ | 575 | $237^{+23}_{-22}$ | $2.46^{+0.08}_{-0.07}$ |
| H | 1787 | $898 \pm 31$ | $1.64 \pm 0.02$ | $2.59 \pm 0.07$ | $13.1^{+0.9}_{-1.3}$ | 787 | $1508^{+192}_{-170}$ | $2.35 \pm 0.05$ |
| B | 4427 | $924^{+17}_{-31}$ | $1.51^{+0.01}_{-0.02}$ | $2.42^{+0.06}_{-0.09}$ | $21.0^{+1.5}_{-4.0}$ | 1088 | $1037^{+86}_{-80}$ | $2.35 \pm 0.04$ |
| Sc | 4149 | $525 \pm 11$ | $1.47 \pm 0.02$ | $2.35 \pm 0.05$ | $6.8 \pm 0.5$ | 405 | $100 \pm 10$ | $2.44^{+0.10}_{-0.09}$ |
| Hc | 2185 | $1060 \pm 31$ | $1.68 \pm 0.01$ | $2.58 \pm 0.07$ | $15.4^{+2.0}_{-1.4}$ | 893 | $1378^{+164}_{-147}$ | $2.30 \pm 0.05$ |
| Bc | 4235 | $842^{+17}_{-31}$ | $1.48 \pm 0.01$ | $2.44 \pm 0.05$ | $18.1^{+1.2}_{-3.0}$ | 994 | $946^{+87}_{-81}$ | $2.38^{+0.05}_{-0.04}$ |

Notes.—Col. (1): X-ray energy band (see Table 1). Col. (2): Number of sources with a hardness ratio of HR < 0. Col. (3): Normalization constant of a broken power law. Col. (4): Faint power-law index of a broken power law. Col. (5): Bright power-law index of a broken power law. Col. (6): Break flux in units of $10^{-15}$ ergs cm$^{-2}$ s$^{-1}$. Col. (7): Number of sources with a hardness ratio of HR > 0. Col. (8): Normalization constant of a single power law. Col. (9): Power-law index of a single power law.

display the redshift distributions of the soft and hard sources in Figure 14. In our sample, 63 ChaMP fields were covered by the optical follow-up survey and 669 of 5515 sources have redshifts, of which we used the sources with S/N > 1.5, matching with optical sources at the highest confidence level, and having the highest confidence level of spectrum identification (for detail descriptions of the optical follow-up survey, spectroscopy, and redshifts in the ChaMP; see Green et al. 2004; Silverman et al. 2005). In all energy bands, the hard sources distribute at lower redshifts than do the soft sources. We performed a KS test (Press et al. 1992) to estimate the probability of soft and hard sources having the same redshift distribution, and it is significantly low (prob $< 1 \times 10^{-4}$) in each energy band.

Since the spectroscopy of the ChaMP sources was biased toward optically bright sources, this bias may affect the X-ray source selection for measuring redshifts and may cause the lower redshift distribution of hard sources: more soft than hard sources selectively have redshifts. In the top panel of Figure 15, we display the hardness ratio distributions of the ChaMP sources in the B (0.3–8 keV) band in the following categories: all sources, sources with optical imaging observations in 63 ChaMP fields, sources having an optical counterpart, and sources having a redshift. In the bottom panel of Figure 15, we display the number ratios of the latter three subsamples over total sample in each hardness ratio bin. Overall, 60% of sources were covered by the optical follow-up survey, of those, 32% of sources have an optical counter-part, and of those, 5% of sources have a redshift. The fraction of sources having a redshift is 5.2% ± 2% for soft sources and 6.7% ± 6% for hard sources. Thus, the bright source selection in the optical band does not significantly affect the X-ray source selection for measuring redshift as a function of hardness ratio.

Then why are hard sources distributed at lower redshifts? Since the quantum efficiency (QE) and the effective area of the *Chandra* ACIS are lower and smaller in the hard band,[10] and because the X-ray source counts are fewer in the hard band than in the soft band when a power-law spectrum is assumed, it is possible to miss more hard sources than soft sources especially at higher redshift. In addition, it is possible that an intrinsically hard source could be observed as a soft source due to the cosmological redshift. In § 5.2.3, we quantitatively investigate this issue in more detail.

#### 5.2.3. *Redshift and Absorption Effects on X-Ray Properties*

To understand the dependence of X-ray properties, such as flux and hardness ratio, on the redshift and absorption, we performed a simple simulation for a test X-ray source using the Sherpa[11] tool. We assumed a power-law model spectrum for the test X-ray source as follows:

$$F(E) = K\left[\frac{E(1+z)}{1\ \mathrm{keV}}\right]^{-\Gamma_{ph}}, \tag{9}$$

where $z$ is the redshift and $\Gamma_{ph}$ is the photon index of the test X-ray source, and $K$ is a normalization constant at 1 keV in units of photons keV$^{-1}$ cm$^{-2}$ s$^{-1}$; we set $K = 0.5$. We assumed a Galactic absorption and intrinsic absorption using Wisconsin cross sections (Morrison & McCammon 1983) as follows:

$$A(E) = \exp\left[-N_{\mathrm{H,Gal}}\sigma(E)\right], \tag{10}$$

$$A(E) = \exp\left[-N_{\mathrm{H,int}}\sigma(E(1+z))\right], \tag{11}$$

where $\sigma(E)$ is the photoelectric cross section not including Thomson scattering, $z$ is the redshift, and $N_{\mathrm{H,Gal}}$ and $N_{\mathrm{H,int}}$ are equivalent hydrogen column density in units of atoms cm$^{-2}$ for the Galactic and intrinsic absorption, respectively. We selected a ChaMP ACIS-I observation whose Galactic absorption is $N_{\mathrm{H,Gal}} = 1.18 \times 10^{20}$ cm$^{-2}$. Using the ancillary response function (ARF) and redistribution matrix function (RMF) files, we calculated the source

[10] See chap. 6 of the *Chandra* Proposers' Observatory Guide, ver. 8.0.

[11] See http://asc.harvard.edu/sherpa/threads/index.html.

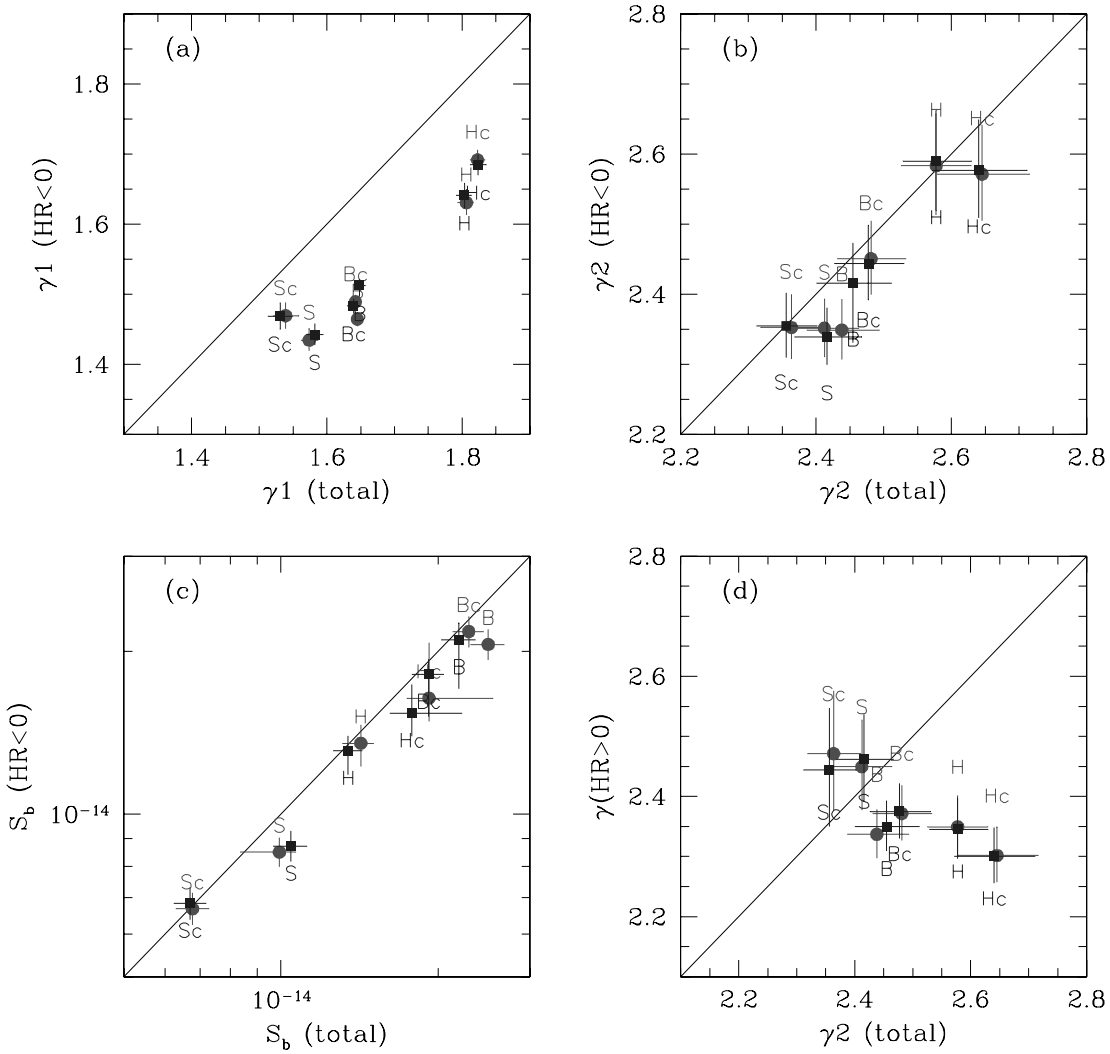


FIG. 13.—Comparison of the best-fit parameters of the ChaMP differential number counts for the total sample (see Table 3) with those for subsamples (see Table 5). The total sample includes all sources regardless of the HR, the soft sample includes sources with HR $< 0$, and the hard sample includes sources with HR $> 0$. (*a*) Faint power-law indices of the total sample vs. the soft sample. (*b*) Bright power-law indices of the total sample vs. the soft sample. (*c*) Break flux of the total sample vs. the soft sample. (*d*) Bright power-law indices of the total sample vs. single power-law indices of the hard sample. The photon indices of $\Gamma_{\rm ph} = 1.4$ (*circles*) and $\Gamma_{\rm ph} = 1.7$ (*squares*) are assumed. The solid line represents the line of equality for the two compared parameters and is shown for illustrative comparison. [*See the electronic edition of the Journal for a color version of this figure*.]

flux and hardness ratio at the aim point for various ranges of redshift ($0 \leq z \leq 10$) and intrinsic absorption ($10^{20} \leq N_{\rm H,int} \leq 10^{24}$ cm$^{-2}$).

In Figure 16, we display the flux-hardness ratio (*S*-HR) diagram in three energy bands. All ChaMP sources with S/N $> 0$ are displayed, and the grid indicates the predicted location of a test source with various redshifts ($z = 0$, 1, 2, and 3) and intrinsic absorption column densities ($\log N_{\rm H,int} = 20, 21.7, 22$, 22.7, and 23.7). A photon index of $\Gamma_{\rm ph} = 1.4$ was assumed for the test source spectrum. We note that the flux of the grid was renormalized to be displayed with the ChaMP scatter plot. The source becomes fainter with increasing absorption and with increasing redshift. The source becomes harder with increasing intrinsic absorption but softer with increasing redshift. In the soft band (0.5–2 keV), this effect is more significant than in the hard and broad bands. From this ideal case study, we can understand the observed flux-hardness ratio diagram in which there are fewer bright hard sources in each energy band (see § 5.2.1). The test X-ray source does not cover the region HR $\leq -0.4$ but will cover this regime when a steeper power-law index (i.e., $\Gamma_{\rm ph} > 2$) is assumed (see Fig. 17).

Figure 17 shows the hardness ratio of the test X-ray source as a function of redshift with a range of intrinsic absorption ($20 \leq \log N_{\rm H,int} \leq 24$) for different photon indices. The test source with steeper power index (i.e., $\Gamma_{\rm ph} = 2$ and 3) covers the soft hardness regime (HR $\leq -0.5$). Again, the test source becomes harder with increasing intrinsic absorption but softer with increasing redshift. For example, in the top left panel (assuming $\Gamma_{\rm ph} = 1.4$), the hard source with $\log N_{\rm H} = 22$ is not observed as a hard source anymore even at $z \sim 1$, and most hard sources are observed as soft sources at $z > 3$. Therefore, a hard source with high redshift is observed as a soft source in the observed frame due to the cosmological redshift, so hard sources with high redshifts are rare (§ 5.2.2). Thus, the hard source number counts do not include high-redshift hard sources, while the soft source number counts include both intrinsically hard and soft sources.

In § 5.2, we found that the hard sources do not show a break in their number count distributions and distribute at lower redshifts compared to soft sources. The soft sources show the break in their number count distributions and distribute from low to high

TABLE 6
BREAK FACTOR

| Band (1) | Total (2) | HR < 0 (3) |
|---|---|---|
| $\Gamma_{ph} = 1.4$ | | |
| B | 0.19 | 0.23 |
| S | 0.21 | 0.24 |
| H | 0.18 | 0.23 |
| Bc | 0.20 | 0.24 |
| Sc | 0.21 | 0.23 |
| Hc | 0.18 | 0.21 |
| $\Gamma_{ph} = 1.7$ | | |
| B | 0.20 | 0.21 |
| S | 0.21 | 0.24 |
| H | 0.18 | 0.22 |
| Bc | 0.20 | 0.25 |
| Sc | 0.21 | 0.23 |
| Hc | 0.18 | 0.21 |

NOTES.—Col. (1): X-ray energy band (see Table 1). Col. (2): Break factor for the total sample. Col. (3): Break factor for the soft sample (HR < 0).

redshifts (see Figs. 12 and 14). The observed soft sources may be a mixture of soft sources and redshifted hard sources (see Fig. 17). These results likely support the suggestion that the hard sources may be preferentially at lower redshifts and so do not show cosmological evolution effects (H03). In addition to H03's suggestion, we suggest that the break in the soft source number counts may be caused by the mixture of X-ray source populations as well as by cosmological evolution effects. To investigate this suggestion, we need redshifts/classifications of the X-ray sources. Since it is not possible to speculate on the distribution of properties

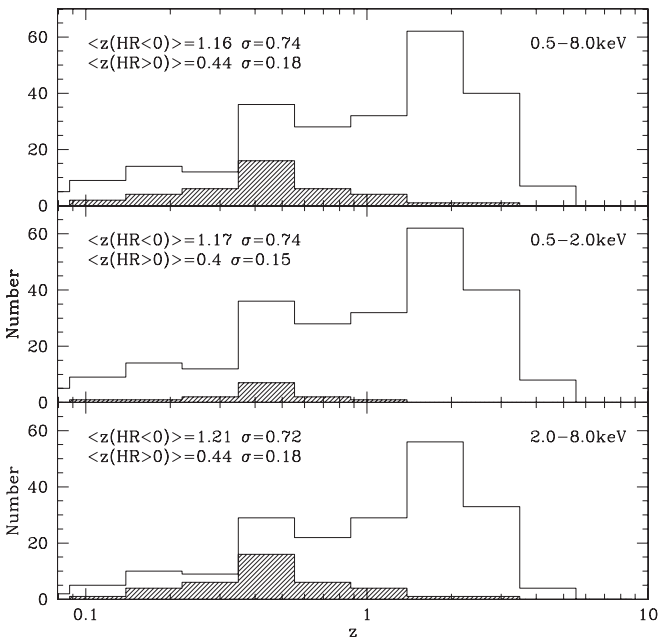


FIG. 14.—Redshift distributions of the soft (HR < 0, *open histogram*) and hard (HR > 0, *hatched histogram*) sources in the Bc (*top*), Sc (*middle*), and Hc (*bottom*) bands. The medians and standard deviations for each distribution are indicated. Hard sources are distributed at lower redshifts compared to the soft sources in all energy bands. Only sources with the highest optical counterpart match confidence levels and with the highest spectrum quality are used.

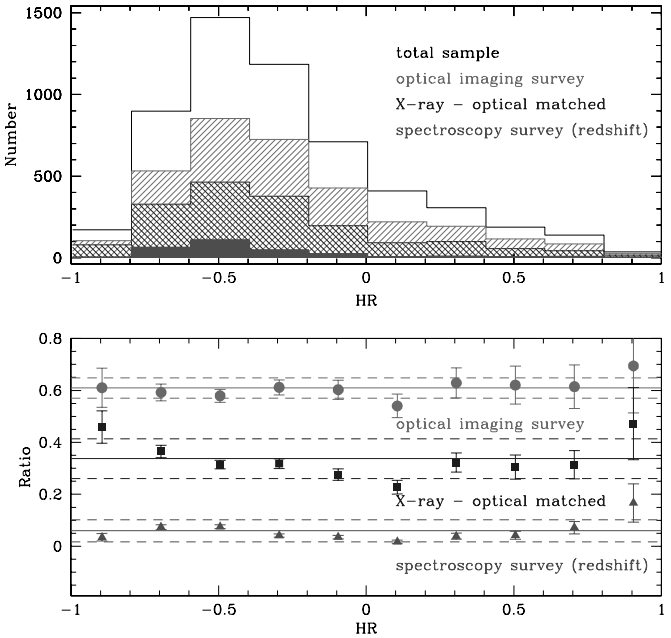


FIG. 15.—*Top*: Hardness ratio distribution of the ChaMP sources in the B (0.3–8 keV) band in the following categories: total sample (*open histogram*), sources in 63 ChaMP fields with optical imaging observations (*gray hatched histogram*), sources having optical counterparts (*black hatched histogram*), and sources having redshifts (*shaded histogram*). *Bottom*: Number ratios of the latter three subsamples over total sample in each hardness ratio bin. The mean (*solid line*) and standard deviations (*dashed lines*) of each ratio are plotted. For the X-ray–optical matched sample and the redshift sample, only sources with the highest match confidence levels and with the highest spectrum quality are used. [*See the electronic edition of the Journal for a color version of this figure.*]

such as intrinsic absorption $N_{H,int}$ from the source counts alone, we need to assume a model for the $N_{H,int}$ distribution of X-ray point sources as a function of redshift and luminosity or to perform X-ray spectral analysis. B04 found that the source density of type 1 AGNs is 10–20 times lower than that of type 2 AGNs at the CDF flux limits in both the 0.5–2 and 2–8 keV bands. They also found that the source density of unobscured/mildly obscured AGNs is 2–3 times lower than those of obscured AGNs at the CDF limits. La Franca et al. (2005) found that the fraction of absorbed ($N_H > 10^{22}$ cm$^{-2}$) AGNs decreases with intrinsic X-ray luminosity but increases with redshift. The fraction of type 1/type 2 AGNs (absorbed/unabsorbed AGNs) probably affects the break in the differential number counts. In addition, since the hard band is less affected by absorption than the soft band, it is possible that the strength of the break is related to the fraction of absorbed sources in each energy band. We expect that further studies could be performed using the ChaMP data once we have more optical/spectroscopy follow-up observations.

## 6. COSMIC X-RAY BACKGROUND

### 6.1. *Resolved Cosmic X-Ray Background Flux Density*

The contribution of discrete sources to the CXRB flux density can be calculated from the differential number counts as follows (M03):

$$F_{\rm resol} = \int_{S_{\rm faint}}^{S_{\rm bright}} \left(\frac{dN}{dS}\right) S'\, dS', \qquad (12)$$

where $S_{\rm faint}$ and $S_{\rm bright}$ are the faint and bright flux limits of the sample.

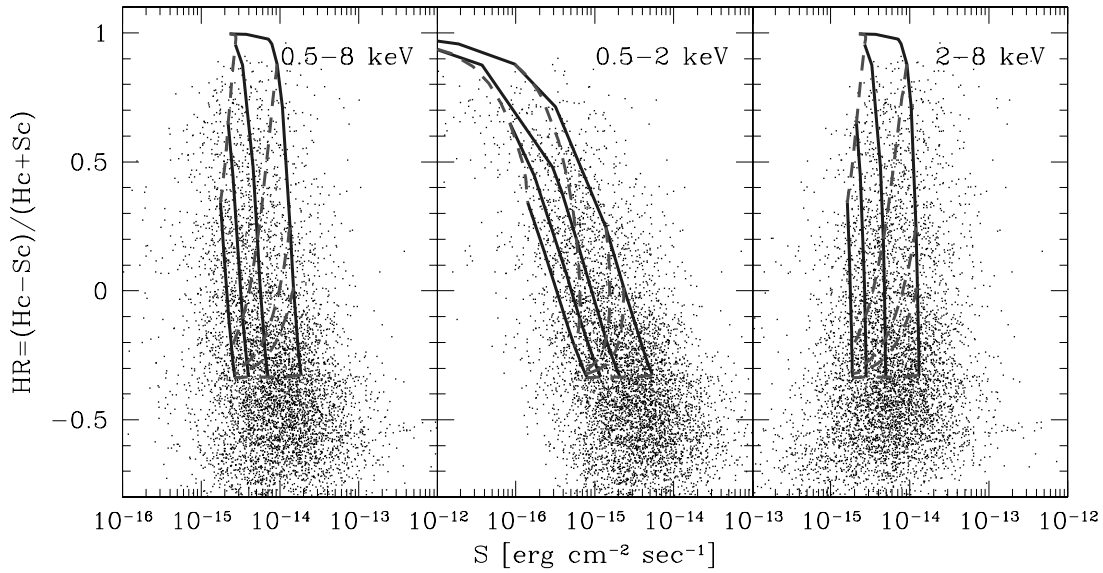


FIG. 16.—Flux-hardness ratio (*S*-HR) diagram for the ChaMP sources with S/N $> 0$ (*black points*) in the 0.5–8 keV (*left*), 0.5–2 keV (*middle*), and 2–8 keV (*right*) bands. The grid indicates the predicted location of a test X-ray source for various values of redshift ($z = 0$, 1, 2, and 3, *solid lines from right to left, respectively*) and intrinsic absorption ($\log N_{\rm H,int} = 20$, 21.7, 22, 22.7, and 23.7, *dashed lines from bottom to top, respectively*). A photon index of $\Gamma_{\rm ph} = 1.4$ was assumed for the test source spectrum. The source becomes fainter with increasing intrinsic absorption and with increasing redshift. The source becomes harder with increasing intrinsic absorption, but softer with increasing redshift. These effects are significant in the soft band. We note that the grid illustrates only a test source to indicate trends but does not cover the full range of the ChaMP sources. [*See the electronic edition of the Journal for a color version of this figure*.]

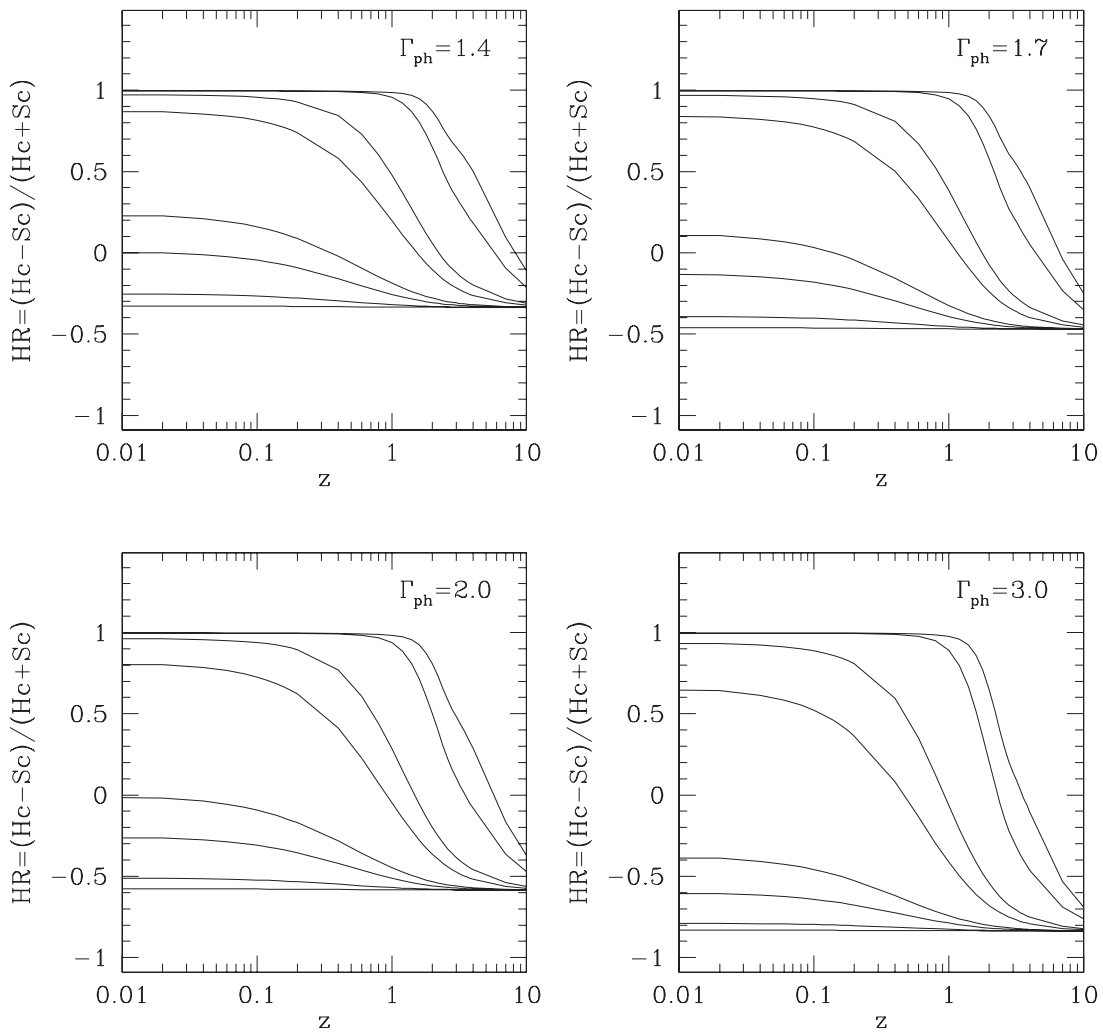


FIG. 17.—Hardness ratio of the test X-ray source as a function of redshift for photon indices of $\Gamma_{\rm ph} = 1.4$ (*top left*), 1.7 (*top right*), 2.0 (*bottom left*), and 3.0 (*bottom right*). In each panel, seven lines represent intrinsic absorptions of $\log N_{\rm H,int} = 20$, 21, 21.7, 22, 22.7, 23, 23.7, and 24, from bottom to top, respectively. The test source becomes harder with increasing intrinsic absorption and with increasing redshift. The intrinsically hard source with high redshift is observed as a soft source in the observed frame due to the cosmological redshift.

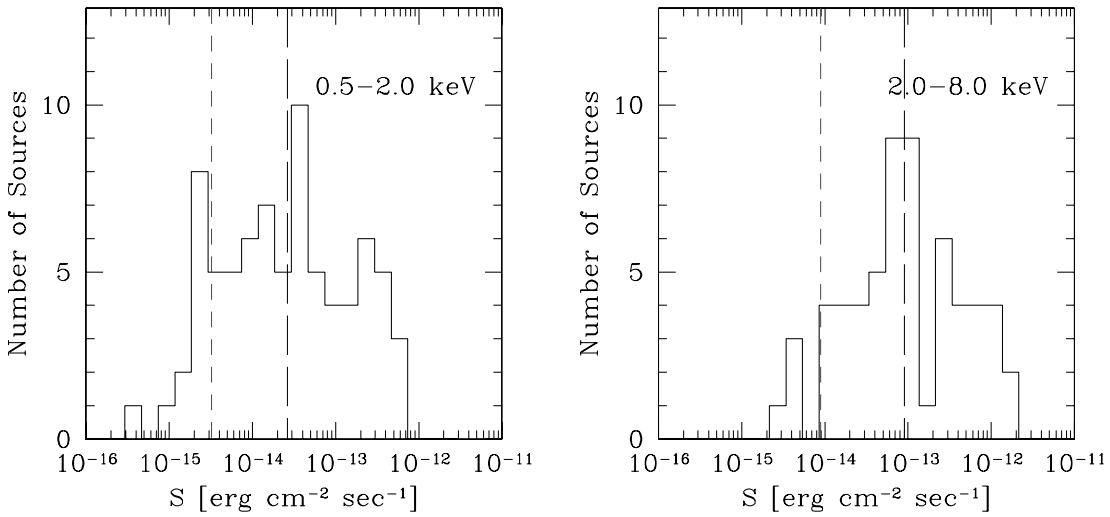


FIG. 18.—Flux distribution of target sources in the Sc (*left*) and the Hc (*right*) bands. The vertical lines indicate the median values of target (*black long-dashed line*) and nontarget (*gray short-dashed line*) sources (see Fig. 1, *left*, and Table 2 for nontarget sources). Target sources have brighter fluxes compared with nontarget sources. [*See the electronic edition of the Journal for a color version of this figure*.]

The ChaMP is a serendipitous *Chandra* archival survey; therefore, most observations contain target sources as intended by the PI and that have brighter flux than nontarget sources as shown in Figure 18. To avoid biased source selection, we excluded target sources for deriving the ChaMP and the ChaMP+CDFs number counts. Even though we have only 85 target sources in total, their contributions to the CXRB flux density are not negligible because of their brightness (M03). Thus, we need to correct for the bright target source contributions to the CXRB. Since the target sources cover a relatively wide flux range, $3 \times 10^{-16}$ to $7 \times 10^{-13}$ (0.5–2 keV) and $2 \times 10^{-14}$ to $2 \times 10^{-12}$ (2–8 keV) ergs cm$^{-2}$ s$^{-1}$, we cannot simply adapt the bright part of the number counts for full sky surveys such as the *ROSAT* All Sky Survey (soft band) or *HEAO-1* A2 extragalactic survey (hard band) that were used by M03 to correct their bright target source contributions to the CXRB. Therefore, we present the lower and upper limits of the resolved CXRB flux density from the ChaMP and ChaMP+CDFs number counts by excluding target sources and including target sources, respectively. We again derived the ChaMP and the ChaMP+CDFs number counts including target sources and list their best-fit parameters in Table 7. Compared with the best-fit parameters without target sources (Table 3), target sources make the bright power-law indices ($\gamma_2$) shallower at 0.9 $\sigma$ confidence, while the faint power-law indices ($\gamma_1$) and break fluxes ($S_b$) show differences at 0.5 and 0.3 $\sigma$, respectively.

Table 8 lists the resolved CXRB flux densities and their contributions to the total CXRB from the ChaMP and the ChaMP+CDFs when the target sources are excluded or included in six energy bands. The average total CXRB flux densities of $(7.52 \pm 0.35) \times 10^{-12}$ (0.5–2 keV) and of $(1.79 \pm 0.11) \times 10^{-11}$ (2–8 keV) ergs cm$^{-2}$ s$^{-1}$ deg$^{-2}$ (B04) are assumed. In the Bc band, the total CXRB flux density is the sum of those in the Sc and Hc bands. The total CXRB flux density in the B, S, and H bands are rescaled from the Bc, Sc, and Hc bands, respectively, by assuming a photon index of $\Gamma_{\rm ph} = 1.4$. In Figure 19, we display the resolved CXRB flux density calculated from the ChaMP+CDFs as a function of flux limit in the Sc and Hc bands, respectively. We plot the resolved CXRB flux densities calculated from the differential number counts with (*black lines*) and without (*dark gray lines*) target sources. The ChaMP sources resolve the total CXRB without (with) target sources at 80% ± 2% (86% ± 2%) and 72% ± 2% (76% ± 2%) in the Sc and Hc bands, respectively. Since the ChaMP+CDFs covers a wider flux range than the ChaMP, the ChaMP+CDFs sources resolve more total CXRB by up to 4%–7% in each band. We extrapolated the best-fit ChaMP+CDFs number counts without target sources down to $10^{-20}$ ergs cm$^{-2}$ s$^{-1}$ and found that the total CXRB is not fully resolved in the soft and hard energy bands within the uncertainties. We note that for the 2–8 keV band, extrapolating the best-fit ChaMP+CDFs number counts with target sources down to $\sim 10^{-17}$ ergs cm$^{-2}$ s$^{-1}$, the total CXRB flux density is fully resolved within the large uncertainties. In Figure 20, we display the difference between the

TABLE 7
LIST OF THE BEST-FIT PARAMETERS INCLUDING TARGET OBJECTS

| Band (1) | $K$ (2) | $\gamma_1$ (3) | $\gamma_2$ (4) | $S_b$ (5) |
|---|---|---|---|---|
| ChaMP Data Set, $\Gamma_{\rm ph} = 1.4$ | | | | |
| S | $753 \pm 15$ | $1.54^{+0.02}_{-0.01}$ | $2.31 \pm 0.04$ | $8.6^{+0.7}_{-0.6}$ |
| H | $1856^{+53}_{-48}$ | $1.81 \pm 0.01$ | $2.48^{+0.05}_{-0.06}$ | $14.0^{+0.9}_{-1.6}$ |
| B | $1550^{+28}_{-48}$ | $1.62 \pm 0.01$ | $2.31 \pm 0.04$ | $21.0^{+4.7}_{-1.6}$ |
| Sc | $610 \pm 12$ | $1.54 \pm 0.02$ | $2.30^{+0.05}_{-0.04}$ | $6.6 \pm 0.5$ |
| Hc | $2038 \pm 50$ | $1.82 \pm 0.01$ | $2.54^{+0.07}_{-0.06}$ | $18.5^{+2.5}_{-2.1}$ |
| Bc | $1561^{+27}_{-50}$ | $1.64 \pm 0.01$ | $2.40 \pm 0.05$ | $22.1 \pm 1.7$ |
| ChaMP Data Set, $\Gamma_{\rm ph} = 1.7$ | | | | |
| S | $766 \pm 15$ | $1.55 \pm 0.01$ | $2.31 \pm 0.04$ | $9.0^{+1.7}_{-0.6}$ |
| H | $1825^{+50}_{-41}$ | $1.82 \pm 0.01$ | $2.48^{+0.04}_{-0.05}$ | $13.5^{+0.7}_{-1.4}$ |
| B | $1469^{+26}_{-41}$ | $1.63 \pm 0.01$ | $2.34 \pm 0.04$ | $19.3^{+3.6}_{-1.4}$ |
| Sc | $615 \pm 12$ | $1.53 \pm 0.02$ | $2.29 \pm 0.04$ | $6.5 \pm 0.5$ |
| Hc | $1930 \pm 47$ | $1.82 \pm 0.01$ | $2.53 \pm 0.07$ | $17.1^{+2.0}_{-2.2}$ |
| Bc | $1410^{+25}_{-47}$ | $1.64 \pm 0.01$ | $2.39 \pm 0.05$ | $18.4^{+1.5}_{-1.4}$ |
| ChaMP+CDFs Data Set, $\Gamma_{\rm ph} = 1.4$ | | | | |
| Sc | $574 \pm 12$ | $1.49 \pm 0.02$ | $2.29^{+0.05}_{-0.10}$ | $6.2^{+0.5}_{-1.4}$ |
| Hc | $1240 \pm 55$ | $1.55 \pm 0.02$ | $2.44 \pm 0.04$ | $11.9^{+0.8}_{-0.7}$ |

NOTES.—Col. (1): X-ray energy band (see Table 1). Col. (2): Normalization constant. Col. (3): Faint power-law index of a broken power law. Col. (4): Bright power-law index of a broken power law. Col. (5): Break flux in units of $10^{-15}$ ergs cm$^{-2}$ s$^{-1}$.

TABLE 8
THE RESOLVED COSMIC X-RAY BACKGROUND FLUX DENSITY

| Band (1) | $f_{min}$ (2) | $f_{max}$ (3) | $CXRB_{total}$ (4) | $CXRB_{nt}$ (5) | $Fraction_{nt}$ (%) (6) | $CXRB_{yt}$ (7) | $Fraction_{yt}$ (%) (8) |
|---|---|---|---|---|---|---|---|
| ChaMP Data Set | | | | | | | |
| B | 0.63 | 0.72 | $2.70 \pm 0.12$ | $2.10 \pm 0.04$ | $77.6 \pm 1.3$ | $2.29 \pm 0.04$ | $84.9 \pm 1.5$ |
| S | 0.33 | 0.33 | $1.10 \pm 0.05$ | $0.82 \pm 0.02$ | $74.7 \pm 1.4$ | $0.89 \pm 0.02$ | $81.5 \pm 1.6$ |
| H | 1.27 | 0.67 | $1.59 \pm 0.10$ | $1.10 \pm 0.03$ | $69.4^{+1.8}_{-1.6}$ | $1.19 \pm 0.03$ | $74.5^{+2.1}_{-1.9}$ |
| Bc | 0.69 | 0.68 | $2.54 \pm 0.12$ | $1.88 \pm 0.03$ | $74.0 \pm 1.3$ | $2.01 \pm 0.04$ | $79.2 \pm 1.4$ |
| Sc | 0.26 | 0.24 | $0.75 \pm 0.04$ | $0.60 \pm 0.01$ | $80.1 \pm 1.6$ | $0.65 \pm 0.01$ | $86.3 \pm 1.7$ |
| Hc | 1.17 | 0.71 | $1.79 \pm 0.11$ | $1.28 \pm 0.03$ | $71.6 \pm 1.7$ | $1.36 \pm 0.03$ | $76.1 \pm 1.8$ |
| ChaMP+CDFs Data Set | | | | | | | |
| Sc | 0.02 | 0.24 | $0.75 \pm 0.04$ | $0.63 \pm 0.01$ | $84.4 \pm 1.6$ | $0.68 \pm 0.01$ | $90.7 \pm 1.9$ |
| Hc | 0.20 | 0.71 | $1.79 \pm 0.11$ | $1.40 \pm 0.03$ | $78.1 \pm 1.8$ | $1.50 \pm 0.07$ | $84.0 \pm 3.7$ |

NOTES.—Col. (1): X-ray energy band (see Table 1). Cols. (2)–(3): Faint and bright flux limits of the data in units of $10^{-15}$ ergs cm$^{-2}$ s$^{-1}$ and $10^{-11}$ ergs cm$^{-2}$ s$^{-1}$, respectively. Col. (4): Total CXRB flux density in units of $10^{-11}$ ergs cm$^{-2}$ s$^{-1}$ deg$^{-2}$. The total CXRB flux densities in the Sc and Hc bands are from B04. The total CXRB flux density in the Bc band is the sum of those in the Sc and Hc bands. The total CXRB flux densities in the B, S, and H bands are rescaled from those in the Bc, Sc, and Hc bands by assuming $\Gamma_{ph} = 1.1$. Col. (5): Resolved CXRB flux density without target sources in units of $10^{-11}$ ergs cm$^{-2}$ s$^{-1}$ deg$^{-2}$. Col. (6): Percentage of the resolved CXRB excluding target sources. Col. (7): Resolved CXRB flux density with target sources in units of $10^{-11}$ ergs cm$^{-2}$ s$^{-1}$ deg$^{-2}$. Col. (8): Percentage of the resolved CXRB including target sources.

resolved CXRB excluding and including target sources, normalizing with that of excluding targets. At bright flux limits, the flux density differences are up to 100%; however, at faint flux limits, the differences are less than 10% in each energy band. The resolved CXRB with and without target sources are upper and lower limits of the resolved CXRB, respectively, and the actual resolved CXRB is between those values. In all energy bands, the fractions of the resolved CXRB increase by 5%–6% when target sources are included.

In Figure 21, we display the resolved CXRB flux density (*top*) and the fraction of resolved CXRB (*bottom*) as a function of faint flux limit in each energy band. Excluding bright target sources, M03 estimated the resolved CXRB flux densities to be $0.69^{+0.03}_{-0.02} \times 10^{-11}$ (0.5–2 keV) and $1.40^{+0.09}_{-0.08} \times 10^{-11}$ (2–8 keV, rescaled from that in the 2–10 keV band assuming a photon index of $\Gamma_{ph} = 1.4$) ergs cm$^{-2}$ s$^{-1}$ deg$^{-2}$, respectively. From the ChaMP+CDFs without target sources, we estimated the resolved CXRB flux density to be $(0.63 \pm 0.01) \times 10^{-11}$ (0.5–2 keV), lower than that of M03 at $2\sigma$ level, and $(1.40 \pm 0.03) \times 10^{-11}$ (2–8 keV) ergs cm$^{-2}$ s$^{-1}$ deg$^{-2}$, in good agreement with M03, respectively. The fractional contributions of the ChaMP+CDFs X-ray point sources excluding (including) target sources to the total CXRB are $84\% \pm 2\%$ ($91\% \pm 2\%$) and $78\% \pm 2\%$ ($84\% \pm 4\%$) in the Sc and Hc band, respectively.

### 6.2. *Total Cosmic X-Ray Background Flux Density*

In § 6.1 we used the measured total CXRB flux density (B04); however, we can also derive the total CXRB flux density from the sum of resolved and unresolved components, using the resolved CXRB estimated from the ChaMP+CDFs. Recently, HM06 measured unresolved CXRB flux densities using the CDF-N and CDF-S of $(0.18 \pm 0.03) \times 10^{-11}$, $(0.34 \pm 0.17) \times 10^{-11}$, and $(0.10 \pm 0.01) \times 10^{-11}$ ergs cm$^{-2}$ s$^{-1}$ deg$^{-2}$ in the 0.5–2, 2–8, and 1–2 keV bands, respectively, after removing all detected point and extended sources in those fields. They also estimated the resolved CXRB flux densities from the CDFs, and from *ROSAT* (0.5–2 keV; Vikhlinin et al. 1995) and from *Chandra*, *XMM-Newton*, and *ASCA* (2–10 keV; M03) for the flux ranges brighter than the CDFs. Then they derived the total CXRB flux densities by adding those resolved and unresolved components.

We derive the total CXRB by adding HM06's unresolved CXRB values to the resolved CXRB of the ChaMP+CDFs. Since these are estimated from a single satellite, *Chandra*, there are no cross calibration uncertainties as in multiple satellite data. In Table 9, we list the resolved, unresolved, and total CXRB flux densities estimated from this and previous studies. For this study, the resolved CXRB in the 1–2 keV band was rescaled from that in the 0.5–2 keV band assuming a photon index of $\Gamma_{ph} = 1.4$. We also provide the total CXRB with and without target sources, which gives lower and upper limits to the total CXRB, respectively. The actual total CXRB is between these two values. The total CXRB flux densities increase by ~6% when target sources are included. Our results agree well with those of HM06 but are lower than earlier numbers, ~80% compared with 90%–94% (M03; B04; see Table 9). Given the large uncertainties in the M03 and B04 studies, they remain marginally consistent (~2 $\sigma$ differences).

We note that, in this study, the total CXRBs include two kinds of unquoted uncertainty. First, the total CXRBs could be overestimated due to the incompleteness correction. The number counts are corrected for incompleteness; however, this corrected portion could also be included in the unresolved CXRB since they are not resolved in the observations. Our resolved CXRBs were corrected for incompleteness by 7% (0.5–2 keV) to 18% (2–8 keV); however, since HM06 used only the central 5′ around each CDF pointing in which the count recovery rate and the detection probability of the source are higher than those at the off-axis region (B04; KM07), the duplicated fraction of the total CXRB is much smaller than the corrected fraction. Second, the total CXRBs could be underestimated since we do not include the resolved CXRB that originates from X-ray extended sources. The resolved CXRB from the *ROSAT* deep cluster survey in the flux range of $10^{-14}$ to $10^{-11}$ ergs cm$^{-2}$ s$^{-1}$ (Rosati et al. 1998) increases our total CXRB flux density by up to 10%, and their contribution to the total CXRB will be 9.5% in the 0.5–2 keV band. We note that, with this extended source contribution, our total CXRB still agrees

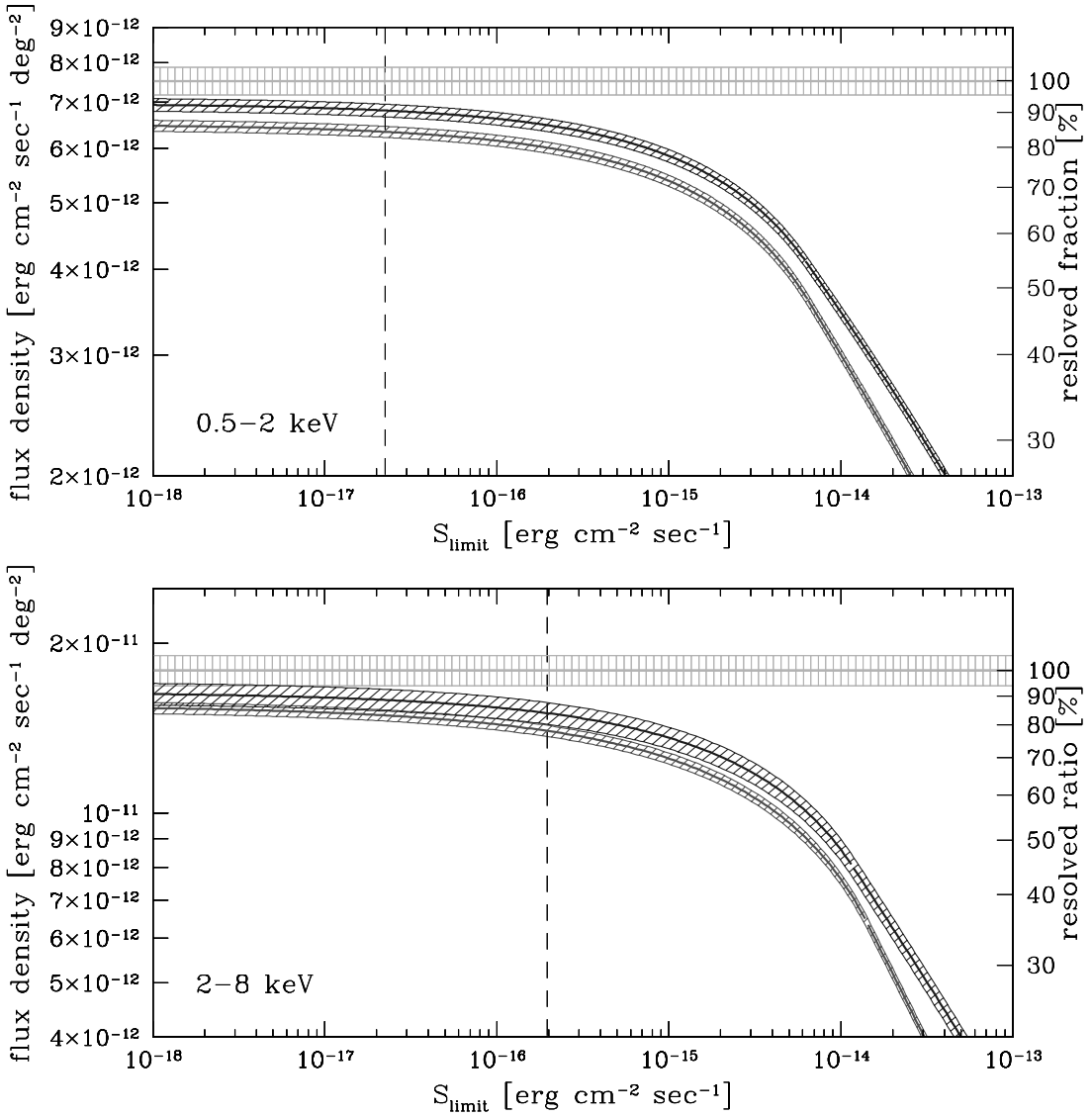


FIG. 19.— Resolved CXRB flux density from the ChaMP+CDFs number counts as a function of flux limit in the 0.5–2 keV (*top*) and 2–8 keV (*bottom*) bands. Black and dark gray shading represents the resolved CXRB with and without targets within $\pm 1\ \sigma$ uncertainties, respectively. The light gray shaded level represents the total CXRB and the $\pm 1\ \sigma$ confidence range from the literature (B04). The vertical dashed line indicates the faint flux limit of the ChaMP+CDFs. Below the faint flux limits, the results are extrapolated. A photon index of $\Gamma_{\rm ph} = 1.4$ was assumed. [*See the electronic edition of the Journal for a color version of this figure.*]

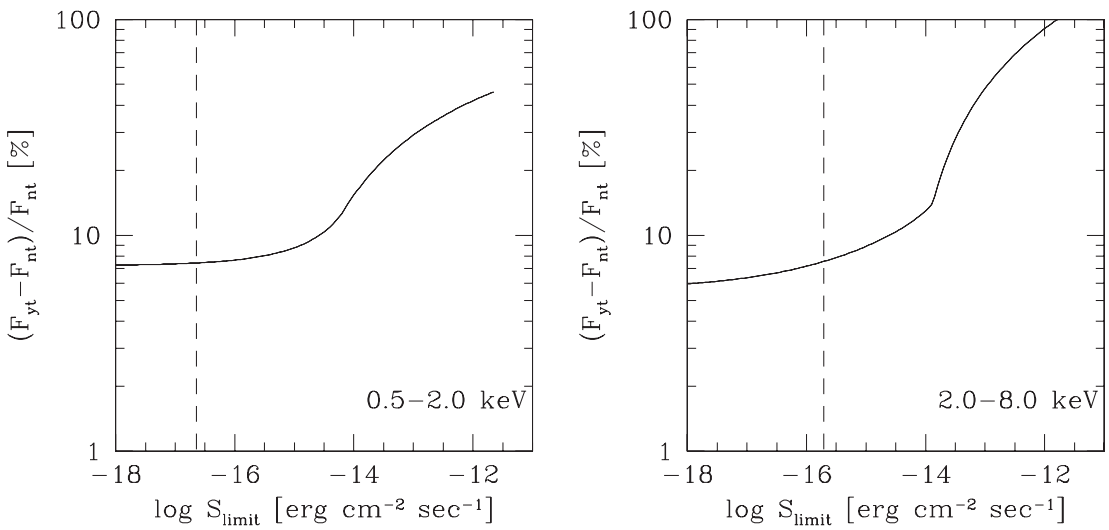


FIG. 20.— Fractional difference between the resolved CXRB excluding ($F_{\rm nt}$) and including ($F_{\rm yt}$) target sources, normalized to that of excluding targets in the 0.5–2 keV (*left*) and in the 2–8 keV (*right*) band. The differences are extrapolated below the faint flux limits (*vertical dashed lines*). At the faint flux limits, the target source fractions are 7% (0.5–2 keV) and 6% (2–8 keV).

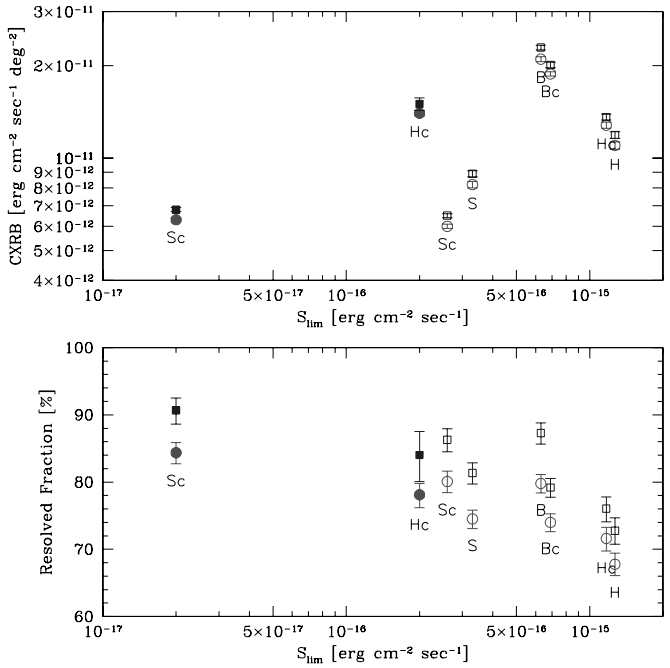


FIG. 21.— *Top*: Resolved CXRB flux density from the ChaMP (*open symbols*) and the ChaMP+CDFs (*filled symbols*) number counts with target (*squares*) and without target (*circles*) as a function of faint flux limit in six energy bands. *Bottom*: Percentage of the total CXRB flux density that is provided by the resolved sources of the ChaMP and ChaMP+CDFs samples. The total CXRB in the Sc and Hc bands are from B04. In other bands, the total CXRB was derived by summing (Bc) or rescaling (B, S, and H) with those in the Sc and Hc bands (see § 6.1). Symbols are the same as the top panel. For the definition of the energy bands, see Table 1. [*See the electronic edition of the Journal for a color version of this figure.*]

with that of other studies within the uncertainties. Meanwhile, so far, there are no number counts for X-ray extended sources in the hard band. Since the spectrum of an extended source is not a simple power law, we cannot rescale the resolved CXRB in the soft band to that in the hard band. Thus, we did not include the extended source contribution to the total CXRB in all energy bands. Since the ChaMP includes extended sources as well (Barkhouse et al. 2006), in a future ChaMP study we expect to determine their number counts in both the soft and the hard bands with higher confidence levels by performing extensive simulations to accurately correct their incompleteness. Then we will be able to estimate the resolved CXRB for extended sources, giving us a self-consistent total CXRB flux density from *Chandra*.

## 7. SUMMARY AND CONCLUSIONS

We present the *Chandra* Multiwavelength Project (ChaMP) X-ray point source number counts in six energy bands. We also present the ChaMP+CDFs number counts in the 0.5–2 and 2–8 keV bands, which cover large flux ranges with small statistical errors. Using these number counts, we measure the resolved and total CXRB flux densities in multiple X-ray energy bands. The main results and conclusions of this study are the following.

1. The number counts of the ChaMP and the ChaMP+CDFs are well fitted with a broken power law. The best-fit faint and bright power indices of the ChaMP+CDFs are $1.49 \pm 0.02$ and $2.36 \pm 0.05$ (0.5–2 keV), and $1.58 \pm 0.01$ and $2.59^{+0.06}_{-0.05}$ (2–8 keV), respectively. The number counts in this study agree with those of previous studies within the uncertainties but are better constrained.

2. In all energy bands, we detect a break in the differential number counts, which is a function of energy band. The origin of the break depending on the energy band can be explained by the identical X-ray population(s) in each energy band.

3. In all energy bands, the soft sources are responsible for the break in the differential number counts. A hard X-ray source becomes softer with increasing redshift, so the hard source number counts do not include high-redshift sources, while the soft source number counts include both soft sources with full range of redshifts and intrinsically hard sources with high redshifts. Therefore, the soft sources show the break due to the cosmological evolutionary effects and mixture of X-ray populations.

4. The resolved CXRB flux densities are measured from the ChaMP and the ChaMP+CDFs number counts in multiple energy bands. We present upper and lower limits of the resolved CXRB by estimating with and without bright target sources.

TABLE 9
THE TOTAL COSMIC X-RAY BACKGROUND FLUX DENSITY

| Band (keV) (1) | Unresolved CXRB (2) | Unresolved CXRB (%) (3) | Resolved CXRB (4) | Resolved CXRB (%) (5) | Total CXRB (6) | Ref. (7) |
|---|---|---|---|---|---|---|
| 0.5–2 | ... | ... | ... | $94.3^{+7.0}_{-6.7}$ | $0.75 \pm 0.04$ | 1 |
| | ... | ... | ... | $89.5^{+5.9}_{-5.7}$ | $0.75 \pm 0.04$ | 2 |
| | $0.18 \pm 0.03$ | $21.9 \pm 3.8$ | $0.63 \pm 0.01$ | $78.1 \pm 1.2$ | $0.81 \pm 0.03$ | 3 |
| | $0.18 \pm 0.03$ | $20.7 \pm 3.6$ | $0.68 \pm 0.01$ | $79.3 \pm 1.2$ | $0.86 \pm 0.03$ | 4 |
| 1–2 | $0.10 \pm 0.01$ | $22.7 \pm 3.1$ | $0.35 \pm 0.02$ | $77.0 \pm 3.0$ | $0.46 \pm 0.03$ | 5 |
| | $0.10 \pm 0.01$ | $21.5 \pm 2.9$ | $0.38 \pm 0.01$ | $78.5 \pm 1.2$ | $0.48 \pm 0.02$ | 3 |
| | $0.10 \pm 0.01$ | $20.2 \pm 2.7$ | $0.41 \pm 0.01$ | $79.8 \pm 1.2$ | $0.51 \pm 0.02$ | 4 |
| 2–8 | ... | ... | ... | $92.6^{+6.6}_{-6.3}$ | $1.79 \pm 0.11$ | 2 |
| | $0.34 \pm 0.17$ | $20.0 \pm 10.0$ | $1.36 \pm 0.10$ | $80.0 \pm 8.0$ | $1.70 \pm 0.20$ | 5 |
| | $0.34 \pm 0.17$ | $19.5 \pm 9.8$ | $1.40 \pm 0.03$ | $80.5 \pm 1.7$ | $1.74 \pm 0.17$ | 3 |
| | $0.34 \pm 0.17$ | $18.5 \pm 9.2$ | $1.50 \pm 0.07$ | $81.5 \pm 3.8$ | $1.84 \pm 0.18$ | 4 |
| 2–10 | ... | ... | ... | $88.8^{+7.8}_{-6.6}$ | $2.02 \pm 0.11$ | 1 |

NOTES.— Col. (1): X-ray energy band. Col. (2): Unresolved CXRB flux density (HM06) in units of $10^{-11}$ergs cm$^{-2}$ s$^{-1}$ deg$^{-2}$. Col. (3): Percentage of the total CXRB flux density that is unresolved. Col. (4): Resolved CXRB flux density from the ChaMP+CDFs number counts in units of $10^{-11}$ ergs cm$^{-2}$ s$^{-1}$ deg$^{-2}$. The resolved CXRB in the 1–2 keV band is rescaled from that in the 0.5–2 keV band assuming $\Gamma_{ph} = 1.4$. Col. (5): Percentage of the total CXRB flux density that is resolved. Col. (6): Total CXRB flux density in units of $10^{-11}$ ergs cm$^{-2}$ s$^{-1}$ deg$^{-2}$. This column is the sum of cols. (2) and (4) for HM06 and this study. Col. (7): Reference.

REFERENCES.—(1) M03; (2) B04; (3) this study without targets; (4) this study with targets; (5) HM06.

5. Excluding target sources, the total CXRB flux densities in units of ergs $cm^{-2}$ $s^{-1}$ $deg^{-2}$ are $(0.81 \pm 0.03) \times 10^{-11}$ (0.5–2 keV), $(1.74 \pm 0.17) \times 10^{-11}$ (2–8 keV), and $(0.48 \pm 0.02) \times 10^{-11}$ (1–2 keV), respectively. Including target sources, the total CXRB flux densities in units of ergs $cm^{-2}$ $s^{-1}$ $deg^{-2}$ are $(0.86 \pm 0.03) \times 10^{-11}$ (0.5–2 keV), $(1.84 \pm 0.18) \times 10^{-11}$ (2–8 keV), and $(0.51 \pm 0.02) \times 10^{-11}$ (1–2 keV), respectively.

6. When the total CXRB estimated from this study is assumed in each band, excluding target sources, the resolved CXRB fractions are 78.1% ± 1.2% (0.5–2 keV), 80.5% ± 1.7% (2–8 keV), and 78.5% ± 1.2% (1–2 keV), respectively. Including target sources, the resolved CXRB fractions are 79.3% ± 1.2% (0.5–2 keV), 81.5% ± 3.8% (2–8 keV), and 79.8% ± 1.2% (1–2 keV), respectively.

We gratefully acknowledge support for this project under NASA CXC archival research grants AR4-5017X and AR6-7020X. P. J. G., D.-W. K., H. D. T., and B. J. W. also acknowledge support through NASA contract NAS8-03060 (CXC). M. G. L. is in part supported by a KOSEF grant (R01-2004-000-10490-0).

REFERENCES

Baldi, A., Molendi, S., Comastri, A., Fiore, F., Matt, G., & Vignali, C. 2002, ApJ, 564, 190
Barkhouse, W. A., et al. 2006, ApJ, 645, 955
Basilakos, S., Plionis, M., Georgakakis, A., & Georgantopoulos, I. 2005, MNRAS, 356, 183
Bauer, F. E., Alexander, D. M., Brandt, W. N., Schneider, D. P., Treister, E., Hornschemeier, A. E., & Garmire, G. P. 2004, AJ, 128, 2048 (B04)
Brandt, W. N., & Hasinger, G. 2005, ARA&A, 43, 827
Cappelluti, N., Cappi, M., Dadina, M., Malaguti, G., Branchesi, M., D'Elia, V., & Palumbo, G. G. C. 2005, A&A, 430, 39
Chiappetti, L., et al. 2005, A&A, 439, 413
Cowie, L. L., Garmire, G. P., Bautz, M. W., Barger, A. J., Brandt, W. N., & Hornschemeier, A. E. 2002, ApJ, 566, L5
Gehrels, N. 1986, ApJ, 303, 336
Green, P. J., et al. 2004, ApJS, 150, 43
Harrison, F. A., Eckart, M. E., Mao, P. H., Helefand, D. J., & Stern, D. 2003, ApJ, 596, 944 (H03)
Hickox, R. C., & Markevitch, M. 2006, ApJ, 645, 95 (HM06)
Johnson, O., Best, P. N., & Almaini, O. 2003, MNRAS, 343, 924
Kenter, A., & Murray, S. 2003, ApJ, 584, 1016
Kim, D.-W., & Fabbiano, G. 2003, ApJ, 586, 826
Kim, D.-W., et al. 2004a, ApJS, 150, 19
———. 2004b, ApJ, 600, 59 (KD04)
Kim, M., et al. 2007, ApJS, in press (KM07)
La Franca, F., et al. 2005, ApJ, 635, 864
Manners, J. C., et al. 2003, MNRAS, 343, 293
Moretti, A., Campana, S., Lazzati, D., & Tagliaferri, G. 2003, ApJ, 588, 696 (M03)
Morrison, R., & McCammon, D. 1983, ApJ, 270, 119
Murdoch, H. S., Crawford, D. F., & Janucey, D. L. 1973, ApJ, 183, 1
Mushotzky, R. F., Cowie, L. L., Barger, A. J., & Arnaud, K. A. 2000, Nature, 404, 459
Park, T., Kashyap, V. L., Siemiginowska, A., van Dyk, D. A., Zezas, A., Heinke, C., & Wargelin, B. J. 2006, ApJ, 652, 610
Press, W. H., Teukolsky, S. A., Vetterling, W. T., & Flannery, B. P. 1992, Numerial Recipes in FORTRAN (Cambridge: Cambridge Univ. Press)
Rosati, P., della Ceca, R., Norman, C., & Giacconi, R. 1998, ApJ, 492, L21
Rosati, P., et al. 2002, ApJ, 566, 667
Silverman, J., et al. 2005, ApJ, 618, 123
Stark, A. A., Gammie, C. F., Wilson, R. W., Bally, J., Linke, R. A., Heiles, C., & Hurwitz, M. 1992, ApJS, 79, 77
Tozzi, P., et al. 2006, A&A, 451, 457
Vikhlinin, A., Forman, W., Jones, C., & Murray, S. 1995, ApJ, 451, 553
Worsley, M. A., et al. 2005, MNRAS, 357, 1281
Yang, Y., Mushotzky, R. F., Steffan, A. T., Barger, A. J., & Cowie, L. L. 2004, AJ, 128, 1501